Master's thesis 2019

Electropolishing of superconducting cavities for quantum memory applications

JANKA BIZNÁROVÁ

CHALMERS
UNIVERSITY OF TECHNOLOGY

Department of Microtechnology and Nanoscience
Quantum Technology Laboratory
Chalmers University of Technology
Gothenburg, Sweden 2019

Electropolishing of superconducting cavities for quantum memory applications
JANKA BIZNÁROVÁ

Supervisor and examiner: Per Delsing, Department of Microtechnology and Nanoscience

Master's Thesis 2019
Department of Microtechnology and Nanoscience
Quantum Technology Laboratory
Chalmers University of Technology
SE-412 96 Gothenburg

Cover: A photograph of the superconducting resonant cavity.

Typeset in LaTeX
Printed by Chalmers Reproservice, Chalmers University of Technology
Gothenburg, Sweden 2019

Electropolishing of superconducting cavities for quantum memory applications
JANKA BIZNÁROVÁ
Department Microtechnology and Nanoscience
Chalmers University of Technology

Abstract

In this thesis, the effect of electrochemical polishing on the internal quality factor Q_i of superconducting resonant cavities, proposed to act as quantum memories, is investigated. The resonant cavities are shaped as $\lambda/4$ resonators with two different outer waveguide lengths, 35 mm and 50 mm. Cavities of both lengths are fabricated from aluminium alloys of two different purities: a 6081 alloy with a 96.3-98.6% aluminium content, and a 4N alloy with a 99.99% aluminium content. Cavities fabricated from the 4N alloy exhibit higher Q_i values than the 6081 Al cavities, both as machined and after several rounds of treatment consisting of chemical etching and annealing, showing the influence of material purity on the quality factor of the resonator.

The electropolishing process implemented in this work has a positive impact on the Q_i of the short cavities, and an adverse effect on the Q_i of the longer cavities. This suggests that the geometry of the electropolishing set-up used here is not optimal for polishing the longer cavities.

The electropolished long cavities display a decrease in low-power Q_i from 12.9×10^6 to 9.9×10^6 for the 6081 alloy, and from 77×10^6 to 25×10^6 for the 4N aluminium. The electropolished short cavities display an increase in low-power Q_i from 5.85×10^6 to 11.5×10^6 for the 6081 alloy, and from 29×10^6 to 94×10^6 for the 4N aluminium. Both short cavities show an increase of the power dependence of Q_i after electropolishing, hinting at an increased dominance of the TLS loss path to the overall energy loss.

Keywords: superconducting resonator, resonant cavity, superconducting cavity, electropolishing, quality factor, quantum memory

Acknowledgements

First and foremost I would like to thank my supervisor, Per Delsing, for entrusting me this project and supporting me on my mission of bridging chemistry and physics. Thank you, Per, for the helpful discussions, and for always finding time when needed, despite balancing the supervision of so many projects.

A big thank you goes to Marina Kudra for the daily supervision, unwavering optimism, and patience while I went on to explore many possibilities. You were the best daily supervisor I could wish for.

I would also like to express my gratitude to Björn Wickman for supporting the electrochemical part of this work, and Gerard Montserrat Sisó for the electrochemistry lab support.

I am also grateful to Anita Fadavi Roudsari for lab support and endless enthusiasm, and David Niepce for brief excursions into materials science and prompt proofreading.

Lastly, I would like to thank everyone at QTL for being so open and welcoming, making this project a genuine pleasure to work on.

Janka Biznárová, Gothenburg, June 2019

Contents

1
Introduction

Ever since proposed by Richard Feynman in the early 1980s[1], the possibility of quantum computation has held the attention of scientists, leading to the proposal of several algorithms capable of efficiently solving hard computational problems. Notable examples of the fruit of these works include Shor's algorithm for integer factorization that shows an exponential speedup compared to the most efficient classical algorithm, or Grover's algorithm, a quantum search algorithm that shows a quadratic speedup.[2] Feynman proposed that a computer based on quantum phenomena would be capable of probabilistic simulation of a quantum system, a task impossible to achieve with a classical computer for sufficiently large quantum systems[1].

The basic unit of information in the field of quantum information processing is a quantum bit (qubit) and is somewhat analogous to the classical binary bit utilized in today's silicon-based computers that encode all information into combinations of two distinct states - 0 and 1. A quantum bit, however, has a peculiar characteristic arising from its quantum mechanical nature - not only can it exist in one of the two distinct states 0 or 1, but also as a quantum superposition of both states at the same time. The word qubit can refer to an actual physical system, as well as an abstract mathematical construct describing a linear superposition of the ground state of the system $|0\rangle$ and an excited state $|1\rangle$. This superposition is expressed as $|\psi\rangle = \alpha\,|0\rangle + \beta\,|1\rangle$, where α and β are complex numbers representing the probability amplitudes of finding the system in the respective state.[2]

This phenomenon is where one of the main strengths of quantum computation - quantum parallelism - comes into play. Lying at the heart of many quantum algorithms, superposition allows the quantum computer to evaluate a function $f(x)$ for multiple values of x simultaneously[2]. This is in contrast to classical parallelism, where multiple circuits are needed to evaluate $f(x)$ for different x in parallel. In quantum computation, this entire action is performed by a single quantum circuit.

Though undoubtedly exciting, the field of quantum computation is not without its struggles. Due to the extreme sensitivity of quantum systems to external perturbations, it is still an ongoing challenge to design satisfactory devices and computational strategies. These include attempts at constructing fault-tolerant algorithms, as well as perfecting quantum circuits to minimize the occurrence of errors. This work contributes to the latter endeavor by investigating the limitations of three-dimensional superconducting resonant cavities, proposed to act as memories for a quantum computer. Aluminium cavities with this architecture have previously been shown to be capable of reaching intrinsic lifetimes of 10 ms at single-photon energies[3]. The cavities are designed to shape resonant fields into a low-loss configuration with the purpose of achieving and sustaining highly coherent Schrödinger cat states and other

similar states. Schrödinger cat states, named in honor of the famous thought experiment constructed by Erwin Schrödinger, are superpositions of macroscopically distinguishable quantum states. A cat state is defined as a superposition of two coherent states with opposite phase[4].

The measure by which the resonant cavities are evaluated is the quality factor Q, which indicates the ratio of energy stored in the resonator and the energy dissipated. Thus, resonators with low power loss and thereby long coherent times are characterized by high values of the quality factor. The aim of this project is to investigate the influence of surface roughness on the quality factor of superconducting resonant cavities.

Electrochemical polishing is proposed in this work as a method of mitigating surface roughness and increasing the Q factor of the resonators. An electropolishing procedure has previously been shown as beneficial for improving the Q factor of superconducting radio frequency niobium cavities[5]. The advantage of employing electrochemical polishing for reducing surface roughness is that it is possible to apply this method to complicated geometries where mechanical polishing methods would be significantly more difficult to apply. Another advantage is that native aluminium oxide is removed from the surface, and the aluminium is passivated with a fresh, uniform layer of oxide. Since the formation of aluminium oxide on an aluminium surface at ambient conditions is inevitable, it is advantageous for the oxide layer to be formed in a controlled manner. Electropolished cavities are compared to cavities that have undergone other treatments (annealing and etching), and effect of these processes on the quality factor of superconducting resonators is investigated.

2

Theory

2.1 Superconductivity

Many materials display zero DC resistance below a certain characteristic critical temperature T_c. This phenomenon, known as superconductivity, typically occurs at cryogenic temperatures (e.g. $T_c(\mathrm{Nb}) = 9.26\,\mathrm{K}$, $T_c(\mathrm{Pb}) = 7.2\,\mathrm{K}$, $T_c(\mathrm{Al}) = 2.1\,\mathrm{K}$). Superconductivity can be experimentally illustrated by measuring the electrical resistance of a material against temperature, as depicted in Figure 2.1 (a).

The absence of resistance in a superconductor is crucial for quantum circuit applications, as the absence of dissipation is one of the necessary conditions for the quantum circuit to reach and maintain its quantum mechanical properties[6]. The electronic signal needs to be able to travel between different points on the chip without energy loss at the qubit operating temperature and transition frequency.

Low temperature is, however, not the only requirement for a superconductor to stay in the superconducting state: superconductivity also breaks down when the material is subject to a magnetic field higher than its thermodynamic critical field H_c, which shows another signature characteristic of superconductors - perfect diamagnetism[7]. In 1933, Meissner and Ochsenfeld found that in addition to denying any magnetic field to penetrate its interior, a superconductor also ejects any field that was flowing through the material before the transition into the superconducting state. This, along with the absence of any and all electrical resistance distinguishes the superconductor from a "mere" perfect conductor, which would trap magnetic field in. This expulsion of magnetic field is referred to as the Meissner effect, and is the underlying reason for the breakdown of superconductivity being at fields exceeding H_c. The thermodynamic critical field H_c is dependent on temperature, as illustrated in Figure 2.1. This characteristic of superconductivity leads to interesting behaviours such as magnetic levitation. Although spectacular to witness and technologically significant, however, magnetic levitation is not especially noteworthy in the context of this work.

A feature that is, however, of special interest here is the existence of the energy gap Δ, described by the BCS theory of superconductivity[7]: below the critical temperature, it becomes energetically favourable for electrons to pair up in so-called Cooper pairs[8]. These Cooper pairs no longer possess fermionic qualities, but rather behave as bosons, thus avoiding the Pauli exclusion principle that forbids two fermions from occupying the same state. Bosons are not required to comply with this restriction, and thus can at very low temperatures occupy the same ground state, forming a condensate. The energy gap that determines the energy needed to

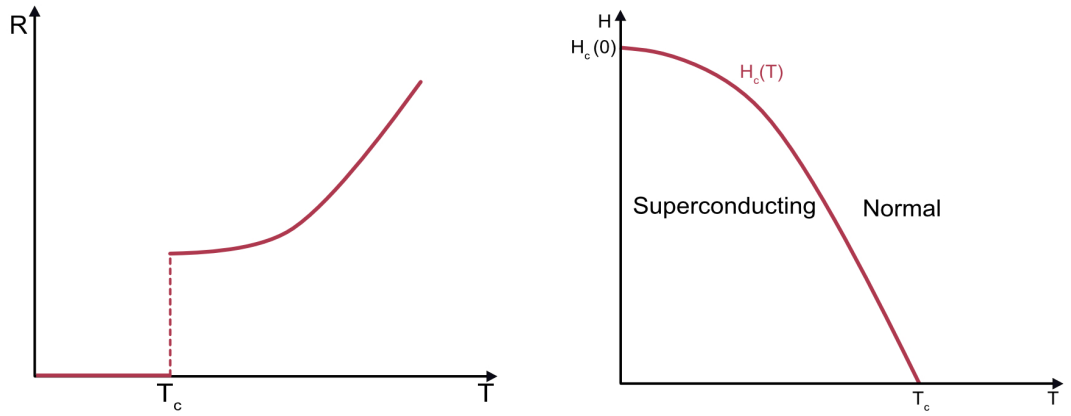

(a) **(b)**

Figure 2.1: **(a)** Superconducting transition at T_c **(b)** The superconducting region, outline by the critical field H_c and critical temperature T_c.

break up a Cooper pair is given by $\Delta = 1.76 k_B T_c$, where k_B is the Boltzmann constant and T_c the aforementioned critical temperature[7].

Here, finally, we reach the connection between superconductivity and the world of quantum mechanics. As was mentioned in the introductory chapter, quantum computation aims to use a quantum system to simulate a quantum system. However, quantum behaviour is usually associated with objects on the nanometer scale. Assigning quantum properties to a bulky, 5 cm tall resonator may therefore feel as counter-intuitive as some ideas behind quantum mechanics themselves. This is where the quantum nature of superconductivity comes into play - a superconducting condensate can be described by a single wave-function, thus lending quantum mechanical properties to bulk materials.

2.2 Cavity QED

Quantum electrodynamics (QED) describes the quantum interaction between matter (atoms and electrons) and electromagnetic fields.[9]

Three dimensional superconducting cavities are expected to be less sensitive to dielectric and conductor losses at surfaces and interfaces than planar resonators, and thus significantly higher quality factors and longer lifetimes should be achievable. Indeed, 3D superconducting aluminium cavity resonators with internal quality factors larger than 0.5×10^9 and intrinsic lifetimes of 0.01 s at single photon energies have been reproducibly achieved[3]. For film resonators the typical quality factors that can be achieved are on the order of 10^6, with corresponding single photon lifetimes between 10-50 µs.[10]

A resonant cavity acts like an electrical harmonic oscillator that can be modelled as a capacitor with a capacitance C and an inductor with inductance L connected in parallel (LC oscillator). The natural frequency of this oscillator is given by $f_r = (2\pi\sqrt{LC})^{-1}$. A quantum harmonic oscillator is characterized by a parabolic potential well with equidistant energy eigenstates separated by $\Delta E = h f_r$.

2.2.1 Losses

Outside of external energy loss paths that are the result of a coupling of the superconducting circuit to the environment, there are a number of internal loss mechanisms that contribute to the overall energy loss. The main loss paths considered in this work are quasi-particle loss, two-level system (TLS) loss, and seam loss.

Quasiparticle loss

According to the two-fluid model of superconductivity, when a superconductor undergoes a transition into the superconducting state ($T < T_c$), the electron population is divided into two parts. One population consists of normal single electrons, known as quasi-particles, subject to scattering and thus exhibiting losses. The other population consists of superconducting electrons paired into Cooper pairs, immune to scattering effects hence exhibiting no loss. Each of these charge carrier populations can carry current; however, in the DC regime ($\omega = 0$), the current follows the path of least resistance and is therefore entirely carried by the Cooper pairs. On the other hand, at high frequencies, a fraction of the current is shunted through the resistive path, which leads to energy dissipation.

The quasiparticle population of a microwave resonator exhibits a strong temperature dependence[11]. Besides thermal excitations, high energy photons with energies higher than the superconducting gap can also acts as sources of quasiparticles by way of breaking up Cooper pairs. A constant influx of such photons (or other energetic particles) can thus sustain a density of non-equilibrium quasiparticles.

TLS loss

The LC model of a resonator assumes an ideal, lossless capacitor. However, at low microwave powers and millikelvin temperatures, dipole relaxation occurs, and the dipoles present within a dielectric can absorb microwave photons, acting as two-level systems (TLS). With increasing probe power, the dipoles can become saturated, and the amount of power absorbed and dissipated by these dipoles decreases.[12]. Saturation of the dipoles can also be thermal in the 20-900 mK range[13].

In an aluminium cavity, aluminium oxide or impurities near the aluminium surface can act as dielectrics contributing to TLS loss.

Seam loss

Superconducting cavities can experience additional loss at points of contact due to imperfect seams. These imperfections stem from surface impurities, microscopic voids at points of contact, or surface oxides[14]. This effect can be mitigated with a careful choice of geometry by placing seams on cavity sites with minimal electromadnetic fields.

2.2.2 Cavity characteristics

The resonant cavity is characterized by its resonance frequency f_r and its quality factor Q. The quality factor characterizes the energy loss of the resonator, and is

defined as the ratio of the energy stored in the resonator to the average energy loss per cycle times 2π.

$$Q = \omega \cdot \frac{\text{Stored energy}}{\text{Dissipated power}} = \omega\tau \tag{2.1}$$

where τ is the energy decay time. Thus, a resonator with lower power loss and longer coherence time is characterized by a higher value of Q.

Fabricating and integrating high quality ($>10^8$) resonators is crucial for their application as coherent quantum memories for cQED[15]. On a path towards optimizing resonators it is important to understand mechanisms limiting their performance, which is an effort this work is aiming to contribute to.

2.3 Electrochemical polishing

Electrochemical polishing (also referred to as electrolytical polishing or electropolishing) is a method of removing surface atoms from a metallic workpiece in order to obtain a polished, passivated and deburred surface.

The simplest electropolishing set-up consists of a working electrode and a counter electrode, both submerged in an appropriate electrolytic solution and connected to a DC voltage source. A schematic of this set-up, applied to the materials used in this work, is depicted in Figure 2.2. The electropolished metal in question, here represented as the working electrode, is connected to the positive terminal of the DC voltage source. The positive voltage turns the metallic workpiece anodic and drives an oxidation reactions at the surface. Cationic species that are a product of this reaction dissolve into the electrolyte and diffuse towards the counter electrode, removing surface defects and irregularities. The counter electrode of an appropriate material is connected to the negative terminal of the voltage source, thus serving as a cathode where the reduction reaction occurs. Ions created by these redox reactions are then driven to the opposite electrode.

The electric circuit is completed by an electrolytic solution. An electrolyte is a chemical compound that upon dissolution in a polar solvent dissociates into anions and cations, producing an electrically conducting solution[16]. The positively charged cations are drawn to the negatively charged cathode, and the negatively charged anions are drawn to the anode. The migration of charged species between the electrodes amounts to a current.[17]

When the electrodes are immersed into the electrolytic bath and no external voltage is applied, a dynamic equilibrium is reached between the redox reactions at the interfaces between the electrolyte and the surfaces of the electrodes. It is only with an applied DC field that the equilibrium shifts in the direction of the oxidation reaction.[17] The driving force for the oxidation reaction is increased by amplifying the applied external DC field, shifting the equilibrium further.

The process of electrolytic dissolution is described by Faraday's laws of electrolysis, which state that the amount of material liberated from the surface of an electrode is proportional to the charge passed, and the amount of different atomic species liberated by a given charge is proportional to their electrochemical equivalent.[18]

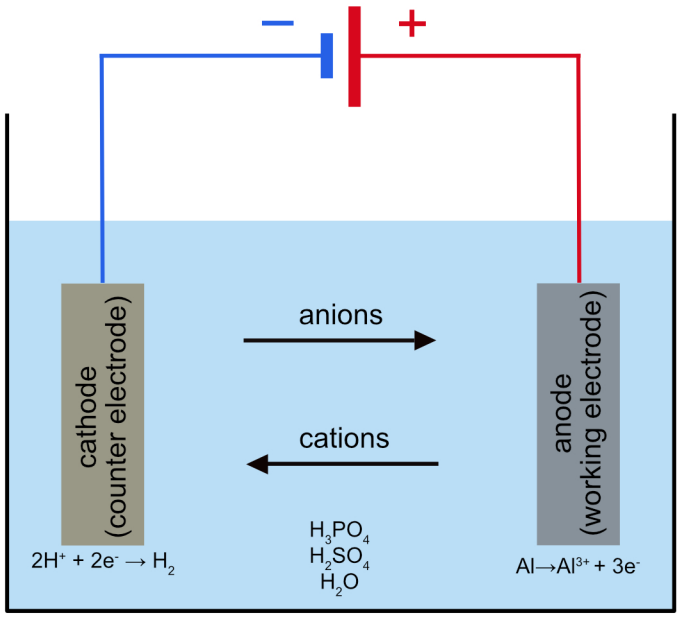

Figure 2.2: A sketch of an electrochemical polishing set-up.

In Faraday's laws of electrolysis, the amount of the liberated material is given by:

$$m = \frac{Q}{F} \cdot \frac{M}{z} \tag{2.2}$$

where m is the mass of the liberated substance, Q is the passed charge, F is Faraday's constant amounting to 96 500 C, M the atomic mass of the dissolving metal (27 for aluminium), and z the valency (3 for aluminium).

While often brushed off with a simple $\mathrm{M} \longrightarrow \mathrm{M}^{z+} + z\,\mathrm{e}^-$, the mechanism of electrochemical dissolution of some materials can be quite complex. The mechanism of aluminium dissolution in an acidic medium passes through the stages of Al_2O_3, $Al(OH)_3$, $Al^{3+} \cdot 6\,H_2O$, and $[AlOH]^{2+}$.[19] The cationic species released by the dissolution or oxidation of the metal then form an adsorbate layer that blocks the surface. These are then solvated by the acceptor anions diffusing to the surface from the dissociated electrolyte, forming complex cations (for example$[AlOHX]^+$ in the case of aluminium, where X is the acceptor species). These cations then dissolve into the electrolyte and are driven by the DC potential towards the cathode. At the cathode a reduction reaction occurs, typically producing hydrogen gas.[20]

On top of the adsorbate layer, a viscous layer is formed over the polished anode.[17] The thickness of the layer is not uniform over the rough surface of the workpiece, resulting in gradients in ohmic resistance between the opposite electrodes. This further contributes to the preferential dissolution of protruding parts as opposed to regions further away from the counter-electrode.

Under certain conditions, electropolishing rate may be limited by diffusive mass transport. The limiting species might be the acceptor species from the electrolyte, water molecules, or most commonly the diffusion of the dissolving metal cation away from the working electrode.[17]

Two fundamentally different mechanisms are distinguished in electrochemical polishing, namely anodic leveling and anodic brightening.[20] Anodic leveling is also referred to as macrosmoothing, as it removes features larger than 1 µm, and anodic brightening is in the same spirit referred to as microsmoothing, as it removes surface features smaller than 1 µm.

Anodic leveling is the more straightforward process generally associated with electropolishing, and its rate can be in many cases predicted quantitatively. The leveling is a result of local concentration of electric field lines, where the material located on the local peaks, closer to the counter electrode is subject to a locally higher potential and is removed preferentially with regards to the material located in valleys.

Anodic brightening, on the other hand, is a process controlled by diffusion, where the oxidized metal ions migrate from small peaks where the diffusion layer is locally thinner, to a lower position. In this way, suppression of crystallographic defects occurs when the atoms are relocated randomly from different crystallographic positions on the surface. If anodic brightening dominates over anodic leveling, a saturation of current despite an increase of applied DC voltage will be observed.[21]

A polarization curve in which an anodic brightening regime has been reached is depicted in Figure 2.3. Four different regimes are indicated in the polarization curve. Chemical etching dominates at low applied voltages until a peak in current is reached (I). Afterwards, a drop in current is usually observed, indicating the formation of a passive layer on the metal surface (II). In the polishing regime (III), the cations diffuse through the stabilized passive layer away from the anodic metal surface. If the applied voltage is increased further (IV), a breakdown of the passive layer as well as pitting of the anodic metal surface occurs.[21]

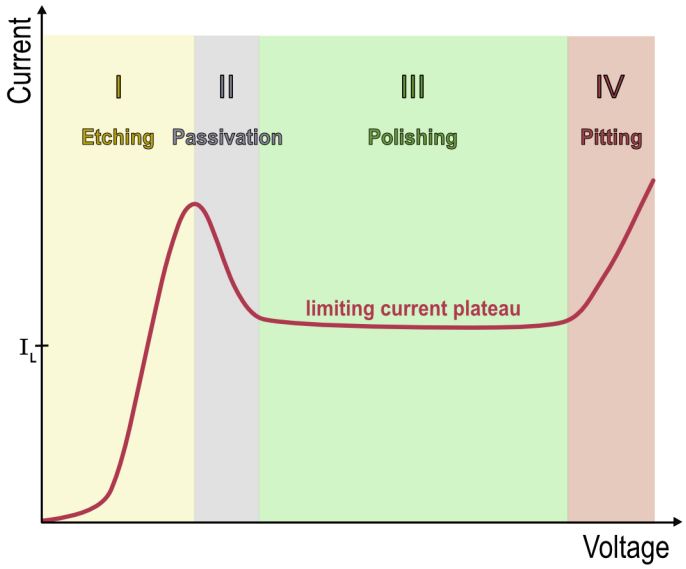

Figure 2.3: Polarization curve of a process where a diffusion-limited anodic brightening regime is achieved. This regime is characterized by a current peak followed by a limiting current plateau.

In principle, it is possible to achieve anodic brightening without anodic leveling and vice versa, but both are present under most experimental conditions.[21]

The final quality of the polished surface is influenced by many conditions, such as the voltage or electric current driving the process, the temperature of the electrolyte bath, hydrodynamic conditions, the geometry of the set-up (e.g. anode-cathode distance) or the length of the electropolishing process.[22]

3
Methods

3.1 Cavity design

The resonant cavities were designed by Marina Kudra at the Quantum Technology Laboratory of the Department of Microtechnology and nanoscience, Chalmers University of Technology.

The cavities were conceived as microwave coaxial $\lambda/4$ resonators, formed by a circular waveguide that is short-circuited on one end and open-circuited on the other.

On resonance, the incident and refected wave creates a standing wave with a certain mode. The fundamental resonance frequency f_0 (the frequency of the lowest mode of excitation) was designed to be around $f_0 \approx 6\,\mathrm{GHz}$. This frequency is determined by the length of the transmission line, created by the inner and outer conductors of the circular waveguide, $l = \lambda/4$, and the next mode of excitation is expected at $f_0 \approx 3\lambda/4$.

The coaxial $\lambda/4$ resonator supports an electromagnetic mode with fields[15]:

$$\vec{E} = \frac{V_0}{r \ln b/a} \sin\left(\frac{\pi y}{2L}\right) \sin(\omega t) \vec{e_r} \tag{3.1}$$

$$\vec{H} = -\frac{V_0}{r\eta \ln b/a} \cos\left(\frac{\pi y}{2L}\right) \cos(\omega t) \vec{e_\theta} \tag{3.2}$$

where V_0 the voltage on the transmission line for $y = L$ and $r = a$, η is the intrinsic impedance of the medium in which the wave propagates ($\eta = \sqrt{\mu/\epsilon}$, where μ is the permeability and ϵ the permittivity of that medium), ω is the frequency of the mode, a is the radius of the inner conductor (the pin with a radius of 1.85 mm), b is the radius of the outer conductor (the cavity wall with a radius of 4.9 mm), r is the length of the radial vector, L the length of the center pin, $\vec{e_r}$ the radial unit vector, and $\vec{e_\theta}$ the tangential unit vector. The y axis is aligned in the direction of the center post in the cavity, with $y = 0$ at the base of the post. The coordinate system is illustrated in Figure 3.2. This description is valid for the coaxial $\lambda/4$ section of the cavity. Above the $\lambda/4$ section, the cut-off frequency of the circular waveguide is lower, and the EM field decays exponentially. This additional waveguide length is added to the to mitigate the effect of the seam loss on Q_i by having the field decay before reaching the seam.

A 3D model of the cavities used in this work is shown in Figure 3.1 (a), and the result of a COMSOL simulation of the electric and magnetic fields of the fundamental

mode of the resonator is shown in Figure 3.1 (b). The model shows how the electric field is concentrated near the top of the center pin, and decays exponentially.

Cavities of two different heights were fabricated, denoted as "long" and short". The only difference between the two designs was the length of the cavity, which was 35 mm for the short cavity and 50 mm for the long cavity. The design for the shorter cavity is illustrated in Figure 3.2. The added length of the outer circular waveguide above the $\lambda/4$ section is to mitigate the effect of seam loss on the top of the cavity where the cavity meets the lid that is placed on the cavity before it is mounted for measuring (see Figure 3.1). The length of the short cavity was designed to be sufficient so that the exponentially decaying electric field was zero at the seam between the cavity and the lid. The additional length in the long cavity was to verify whether this length is indeed sufficient.

A circular opening was made in the side of the cavity, serving as a waveguide for the microwave signals used to apply excitations to the cavity. Through this opening, the cavity was coupled to the center pin of a coaxial cable that served as both input and output. The strength of the capacitive coupling between the cavity and the center pin was adjustable by varying the length of the pin, where longer pin lengths led to weaker coupling, and shorter pin lengths to stronger coupling.

The material used for the fabrication of the cavities was aluminium. Aluminium is a commonly used material in superconducting circuits, as its critical temperature T_c of 1.2 K is sufficient to satisfy the $k_B T << \hbar\omega_{01}$ and $\hbar\omega_{01} << \Delta$ conditions necessary for operating a quantum circuit, where $\hbar\omega_{01}$ is the transition energy between the ground state and the first excited state, and Δ is the energy gap of the material[6].

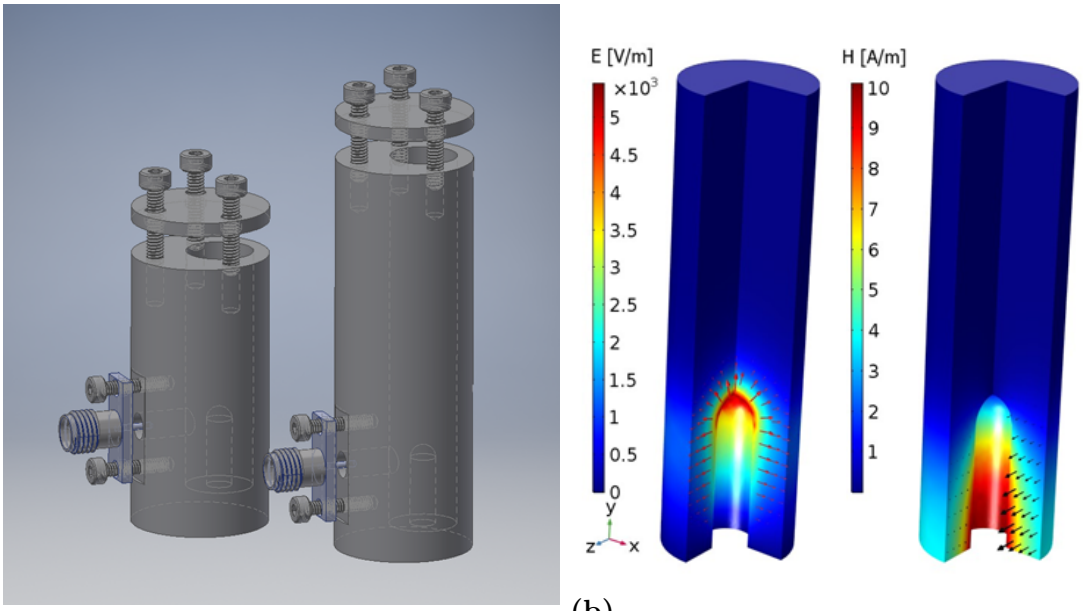

(a) **(b)**

Figure 3.1: **(a)** the "long" and the "short" cavity, closed by the 4N aluminium lid, and equipped with a coupling pin. **(b)** Simulation of the fundamental (lowest frequency) mode of the cavity.

The cavities were machined from bulk aluminium of two different purities. The purest, denoted as 4N, contained 99.99% of aluminium. Another grade of aluminium used was the 6081 aluminium alloy that contained 96.3-98.6% of aluminium. The majority of the remainder of the content is silicon (0.7-1.1%) and magnesium (0.6-1.0%).

The lids placed on the cavities before mounting were all made with 4N aluminium.

Aluminium has a high affinity to oxygen, and its exposure to most environments results in a protective oxide film that shields the bulk metal from further exposure[23]. Aluminium oxide is not superconducting and is a known host of dielectric loss in superconducting circuits[24], therefore efforts are made to keep the oxide clean and the thickness of the oxide layer at a minimum.

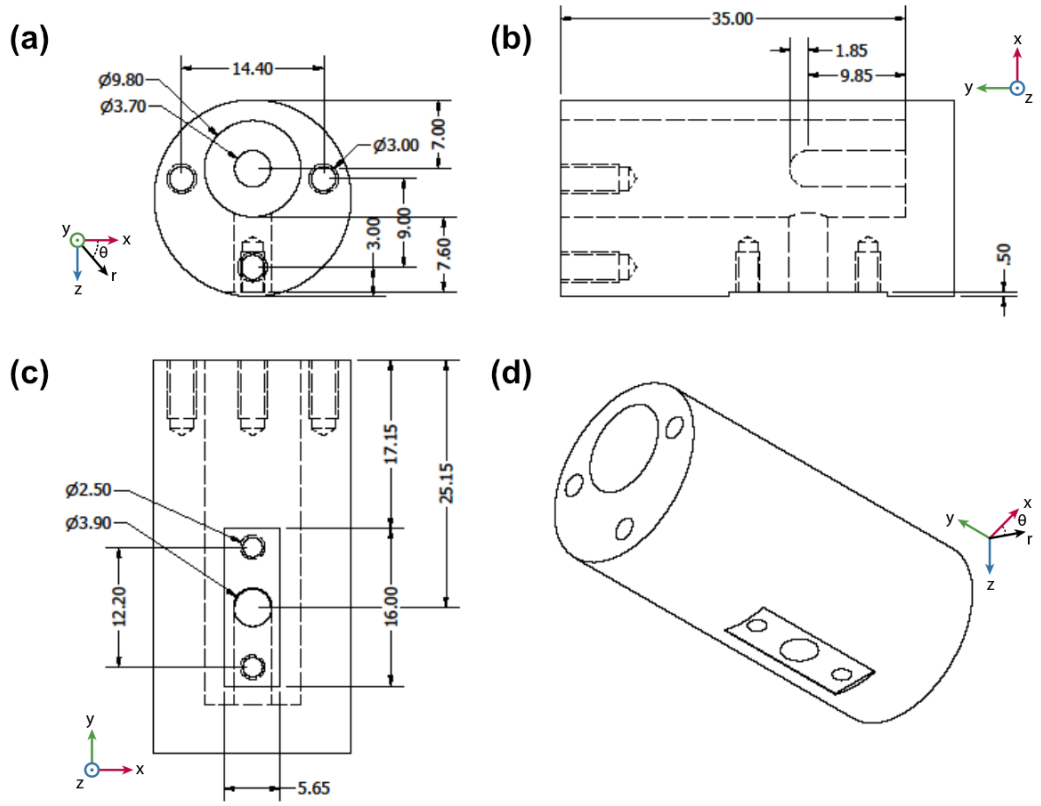

Figure 3.2: Design of the "short" cavity. **(a)** Top view of the cavity and its center pin, forming a circular coaxial waveguide. Also pictured are three screw holes for mounting the cavity inside a cryostat. The dotted lines indicate the position of input-output coupling waveguide, which is present in a lower part of the cavity. **(b)** Side view, showing the curved center pin of the resonator waveguide, the length of the waveguide (35 mm here and 50 mm for the "long" cavities), the input-output waveguide, and screw holes. The input-output waveguide is a circular opening in the side of the cavity, facing the center pin. It is depicted in the bottom part of this drawing, between two screw holes for mounting the coupling pin. **(c)** Another side view, showing the input-output waveguide facing the center pin. **(d)** A view of the cavity's exterior. A rectangle around the input-output waveguide is made flat to accommodate the mounting of the coupling pin.

3.2 Electropolishing

The most common electrolytes used in electropolishing are highly viscous concentrated acid solutions such as sulphuric acid, phosphoric acid and their mixtures, or solutions made of perchloric and acetic acid[20]. Since perchloric acid is volatile and a cooling system would be necessary for polishing in this acid, a mixture of sulphuric and phosphoric acid was selected as an electrolyte. An interesting aspect of using this mixture for electropolishing aluminium is that phosphoric acid has a high affinity towards attacking aluminium oxide[25]. This might prove especially beneficial for the superconducting circuit application, where minimizing surface oxide thickness is desirable.

Based on publications that found this ratio optimal for the electropolishing of aluminium, the chosen electrolyte consisted of 60% phosphoric acid and 40% sulphuric acid with no additional solvents[19,21]. The reports on the optimal temperature of aluminium electropolishing in this electrolyte vary, therefore several temperatures were investigated.

The electrolytic solutions were mixed from batch solutions of sulfuric acid with a concentration of 96% and orthophosphoric acid with a concentration of 85%. Pure phosphoric acid is solid at room temperature, and in concentrations higher than 85% is highly viscous and has a tendency to oligomerize into polyphosphoric acids[26], which is why this particular purity is used here.

Before experimenting with the resonant cavities, flat aluminium testpieces were used in order to understand and optimize the process.

Subsequent to every electrochemical procedure, all samples were rinsed in deionized water and dried under a stream of nitrogen gas. For cavities, after the last electropolishing procedure before being mounted in a dilution refrigerator for Q measurements (as described later in this chapter), an additional cleaning procedure was carried out inside a cleanroom facility. In this procedure, cavities were solvent cleaned in acetone at room temperature for 5 minutes under ultrasonic agitation, then with isopropanol under the same conditions, and dried under a stream of nitrogen gas.

3.2.1 Set-up

In the electropolishing set-up, the aluminium workpiece was connected to the positive voltage terminal of a potentiostat in order to be made anodic. A graphite rod was connected to the negative terminal, serving as a counter-electrode.

The glass vessel containing the electrodes and electrolyte was doubly walled (see Figure 3.4, allowing for water to circulate in the outer jacket, which was used to keep the electrolyte at a constant temperature of 30 °C,50 °C, or 60 °C with a circulation thermostat.

A reference electrode was added to the set-up for certain measurements, completing the so-called three-electrode set-up. A circuit representation of this set-up is depicted in Figure 3.3.

Reference electrodes are used in electrochemistry to bypass the impossibility of a direct measurement of the Galvani potential difference between an electrode and

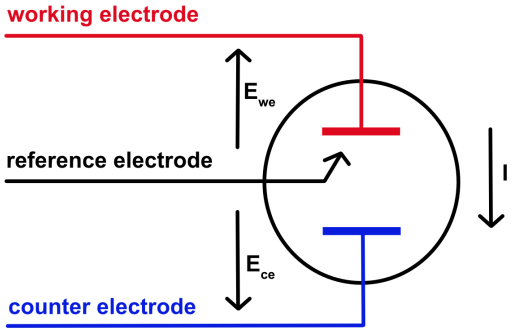

Figure 3.3: Circuit diagram of the three-electrode setup. E_{we} and E_{ce} are the measured overpotentials towards the working electrode and counter electrode, respectively.

the electrolyte. To measure this difference, a voltage probe would have to be in contact with both phases at the same time. However, submerging any probe into the electrolyte and putting it in contact with the metal electrode will result in a second phase boundary between the probe and the electrolyte, forming another electrochemical equilibrium with its own Galvani potential difference. The overall potential difference measured by this probe would thus be the difference between the Galvani potentials of the two interfaces, and not between the electrode and the electrolyte itself.[16]

Therefore, another electrode with a known and stable equilibrium electrode potential (defined with respect to the standard hydrogen electrode) is introduced into the set-up. This electrode is only in contact with the electrolytic solution, and no external potential or current is applied to it. Instead, the potential of the working or counter electrode in reference to this electrode is measured.

Using a reference electrode is thus not strictly necessary for applying constant external voltage between two electrodes and measuring the passing current, as was often done in this work. However, including a reference electrode in a set-up is still useful for obtaining precise information about variables such as the open circuit potential of the system, therefore it was included in the set-up whenever possible.

A saturated calomel reference electrode (SCE) was used as a reference in this work. In this type of reference electrode calomel, a sparingly soluble Hg_2Cl_2 salt, floats on top of a liquid mercury drop in a saturated KCl solution. The potential-determining reaction for this electrode is $Hg_2{}^{2+} + 2\,e^- \longrightarrow 2\,Hg$ upon the dissociation of calomel into $Hg_2{}^{2+}$ and Cl^- in the KCl solution[16].

3.2.1.1 Flat testpieces

The flat testpieces were 99.99% aluminium quarter-discs with a 2 cm diameter. To serve as a working electrode, the samples were attached to a metallic wire using a copper tape and insulated with hot glue on the backside. The glue was used not only to protect the copper tape from being attacked by acid, but also to shield all

aluminium sites not directly facing the counter electrode, so as to not affect the measurements.

The three-electrode set-up was used to carry out these measurements. The set-up and samples can be seen in Figure 3.4. Magnetic stirring was used to aid the heating of the electrolyte, as well as to keep the concentration of the electrolyte uniform.

For a short experiment with ultrasonic agitation, proposed to combat the effects of the oxygen evolution, the vessel was immersed in an ultrasonic bath.

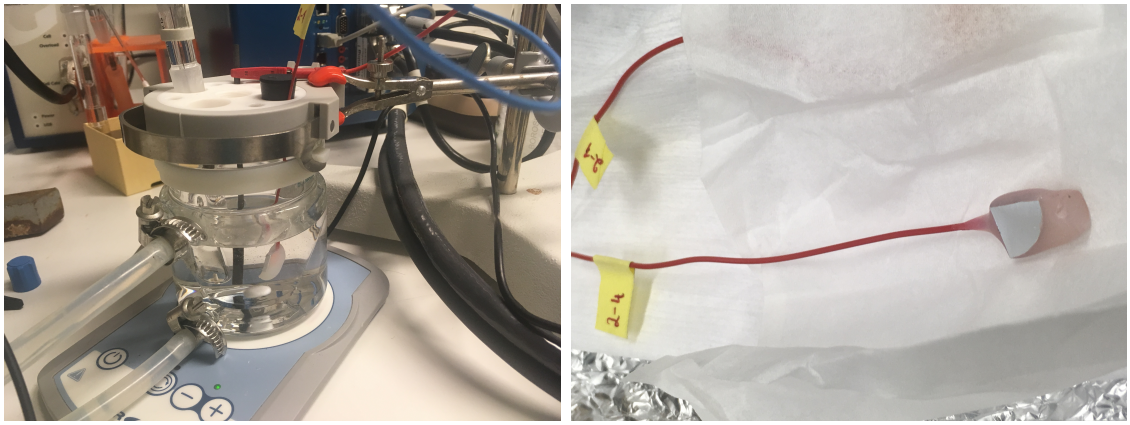

(a) **(b)**

Figure 3.4: **(a)** The three-electrode set-up for electropolishing aluminium testpieces. SCE reference on the left, graphite rod as a counter electrode in the center, and aluminium testpiece as a working electrode on the right. **(b)** Aluminium testpiece, prepared as a working electrode.

3.2.1.2 Cavities

The protection of the outside surface of the cavity was more elaborate than for the flat samples, as experiments have shown that the previous method was insufficient in protecting the copper tape from being attacked by the acid. Protecting the tape is of utmost importance, as copper is readily oxidized by both sulfuric and phosphoric acid and can deposit on the aluminium surface. Copper is not superconducting, so its deposition on the aluminium surface is highly undesirable as it leads to the degradation of the quality factor at cryogenic temperatures.

The winning strategy for protecting the tape was to cover it with vinyl insulating tape, hot glue, and kapton tape. Kapton is a polyimide film with high resistance to sulphuric and phosphoric acid. Later on, the copper tape was replaced by aluminium tape. The aluminium tape was shielded from the acid in the exact same manner as copper tape was, since the deposition of impurities from the tape in the event of an acid breach was equally undesirable as before. Each step of the outer surface coating is captured in Figure 3.5.

No stirring was used in polishing the cavities, as the geometry of the set-up did not allow for it, as can be seen in Figure 3.6.

The geometry of the set-up proved problematic for the integration of the reference electrode as well. A reference electrode should be placed as close to the site exposed to the working electrode as possible. This was, however, not possible here,

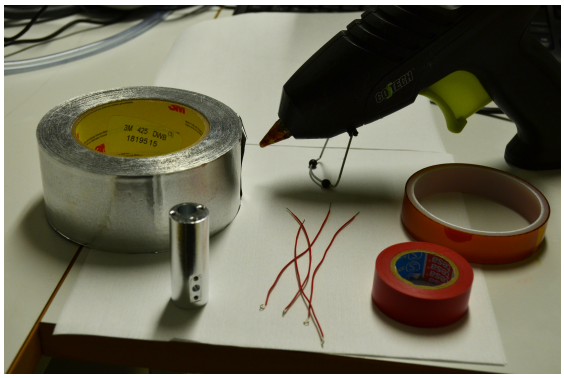

(a) Electrode components

(b) Bare aluminium cavity

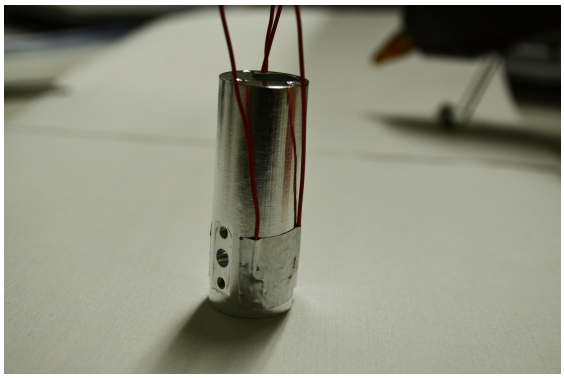

(c) Metallic wires and aluminium tape

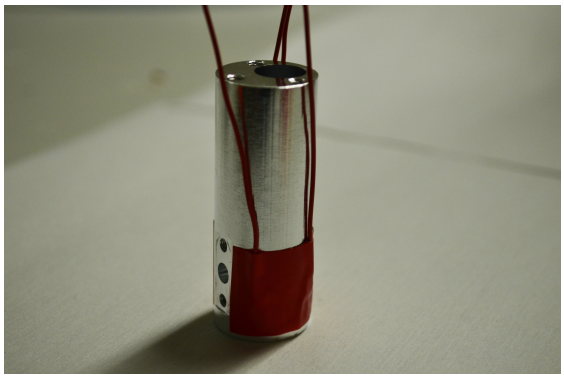

(d) Electrical insulation tape

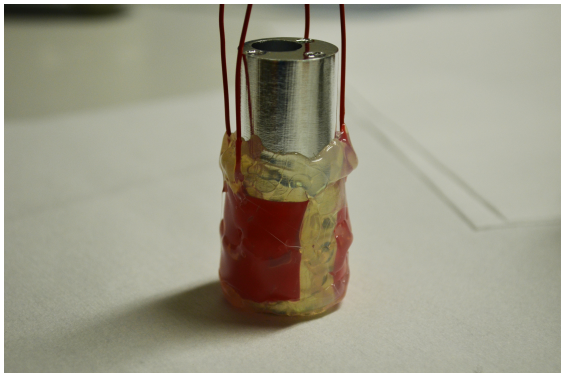

(e) Hot glue coat

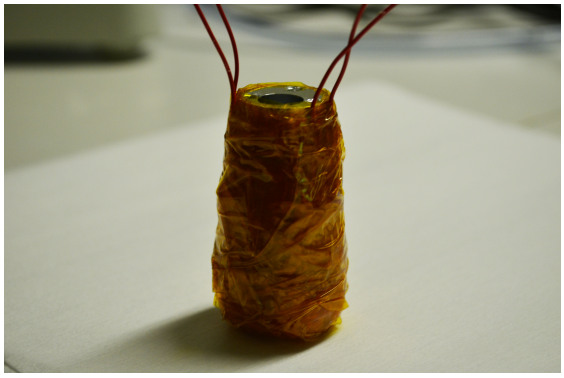

(f) Kapton tape coat

Figure 3.5: Protection of the outer aluminium surface, as well as of the wires and aluminium tape used to apply external potential to the aluminium workpiece.

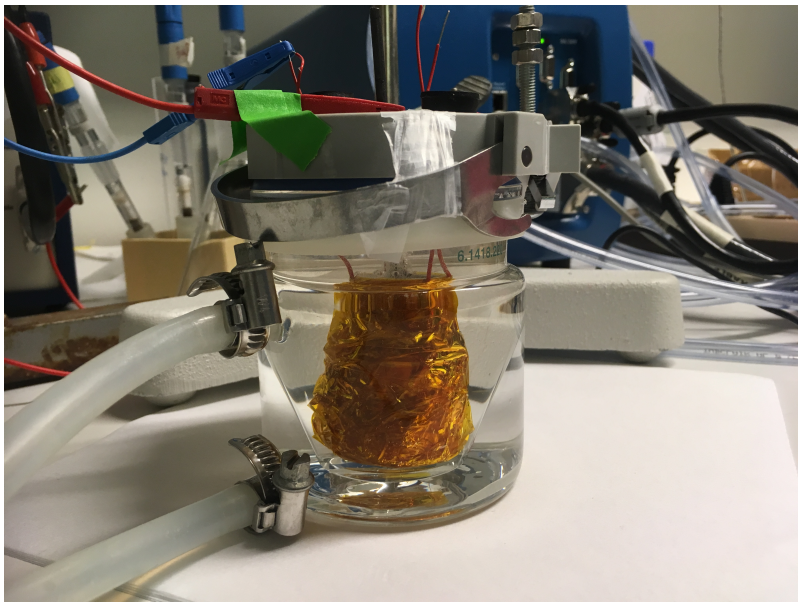

Figure 3.6: Cavity electropolishing setup. The graphite rod counter electrode is submerged in the center of the cavity, carefully aligned to avoid direct contact with the aluminium surface.

as the reference electrode had to be placed outside of the cavity, close to the surface protected by several layers of different materials. This led to inaccurate results, and the reference electrode was omitted from the cavity electropolishing set-up.

3.2.2 Linear sweep voltammetry

Linear sweep voltammetry (LSV) was used to determine the conditions at which the different electropolishing regimes are present by studying the obtained polarization curve. To measure a polarization curve, a voltage sweep is performed at a defined sweeping rate while the current passing between the electrodes is recorded (see Figure 4.1). Different sweep rates were investigated to verify the presence of the diffusion limited regime, and to observe the shift of the limited current plateau in the voltage spectrum with changing sweep rates.

In flat testpieces, the sweeps were initiated after the open circuit voltage E_{oc} stabilized. In cavities this proved to be counter-productive. With no external potential applied, chemical etching reactions took place, resulting in tides of gaseous product rising from the surface of the aluminium workpiece. If left uninterruped for too long, the etching became quite violent, preventing the diffusion layer from establishing properly for the polishing process to take place. In this case, the cavity had to be taken out of the electrolyte solution and rinsed in deionized water to restore the aluminium surface. This exposure to water and atmospheric oxygen between different LSV cycles was undesirable, as it could alter the starting conditions of the individual sweeps, affecting measurement results. Furthermore, due to the constrained geometry of the cavity electropolishing set-up (Figure 3.6), re-introduction of the cavity into the vessel after removal had to be performed without the presence of the electrolyte. The cavity and the graphite rod needed to be properly aligned to avoid

direct contact, which needed to occur outside of the acidic environment to avoid the aforementioned etching. This was at odds with safety procedures concerning the handling of hot acids.

With these aspects in mind, removing and rinsing the cavity every time the etching went out of control was evaluated as undesirable. The individual sweeps were therefore started as soon as the bubbling of the aluminium etching product was observed, regardless of whether the E_{oc} had stabilized.

3.2.3 Chronovoltammetry and chronoamperometry

After choosing a suitable voltage or current from the polarization curve obtained from the LSV measurements, the electrochemical polishing itself can be performed by keeping the chosen variable constant for a selected time period. In chronovoltammetery, the current passing between the working and counter electrodes is kept constant, while the voltage developed between the electrodes is recorded. In chronoamperometry, a constant voltage is applied between the electrodes while the passing current is recorded.

In some experiments, LSV was combined with chronoamperometry to ensure the presence of the limited current regime. In those cases, a sweep was performed until a voltage selected based on previous sweeps was reached. Upon reaching the desired voltage, a chronoamperometry measurement was initiated, keeping the selected voltage constant for a specified amount of time.

3.3 Etching

Etching is another chemical surface processing technique investigated here in connection with improving the Q of superconducting resonators. A comparison of the effect of this method on the Q to the effect of the more elaborate electropolishing process was of special interest.

The chemical etching method removes material from the surface by dissolution in a strongly corrosive substance, known as etchant. Surface oxide and other materials that may have deposited on the surface are removed, allowing for the formation of a fresh layer of oxide. No external electrical potential is applied here, but the surface roughness could nevertheless be improved if a local saturation by the etching reaction products occurs in the valleys. This could lead to a mismatch in kinetics of dissolution at peaks as opposed to valleys and thus result in a flatter surface.

The aluminium etchant used to etch the cavities consisted of phosphoric acid, acetic acid, nitric acid and water with mass ratios indicated in Table 3.1. An etchant of a comparable composition had previously been shown to have aided in the fabrication of 3D superconducting cavities with Q_i on the order of 0.5×10^9.[3]

Phosphoric acid	60%
Acetic acid	3.5%
Nitric acid	2.5%
Water	34%

Table 3.1: Composition of the Aluminium etchant

In this etchant, nitric acid (HNO_3) serves for the oxidation of aluminium, phosphoric acid (H_3PO_4) for the oxidation of aluminium oxide (Al_2O_3), acetic acid (CH_3COOH) for buffering and water for dilution and etch rate control[25]. The process starts with the phosphoric acid mediated dissolution of the few nanometers thick native Al_2O_3 layer that is inevitably present on every Al surface. Subsequently, the processes of Al oxidation by HNO_3 and the resulting Al_2O_3 oxidation by H_3PO_4 alternate, leading to the following overall chemical balance[15]:

$$7\,Al + 5\,HNO_3 + 21\,H_3PO_4 \rightarrow 7\,Al(H_2PO_4)_3 + 13\,H_2O + 2\,N_2 + NO_2 \tag{3.3}$$

The etching process is exothermal and the etch rate is strongly dependent on temperature. Two methods were used here: etching with hot acid and room temperature etching. Both were performed inside a cleanroom facility. The screw holes in the cavity were covered with titanium screws so that the threads would be protected from the etchant. Titanium was chosen because it is heavily resistant to the solution[25]. Hot etching was performed inside a fume hood, where a beaker with etchant was placed on a hot plate with a temperature sensor immersed in the solution. The solution was unstirred. Once the etchant solution reached 50 °C, the cavity was placed inside and left to etch for 2 hours. The set-up can be seen in Figure 3.7. After 2 hours the cavity was taken out of the solution and submerged into water, a fresh etchant was heated up to 50 °C and the cavity was submerged for another 2 hours.

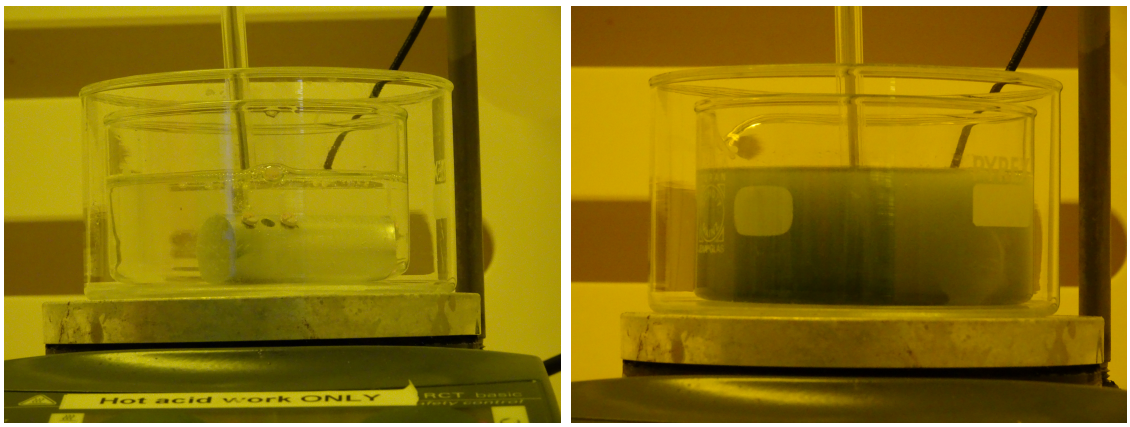

(a) **(b)**

Figure 3.7: Etching solution **(a)** right after the immersion of the aluminium cavity and **(b)** after 2 hours of of etching at 50 °C.

The 4 hours of etching in total removed approximately 150 µm of material from the cavity surface, according to the etch rate of 100 Å s^{-1} estimated for this etchant at 50 °C.[25] The refreshment of the etchant mid-process was done in order to avoid saturation of the solution by the reaction products. In Figure 3.7 the transparent solution immediately after the submersion of the cavity can be observed (a), as well as the dark green color the solution assumed after 2 hours of etching (b). This green tint is due to the aluminium phosphate salt (see eq. 3.3).

Room temperature etching was performed on a ventilated wet bench. The etching time for this method was much shorter, 20 minutes with the samples being lifted out of the etchant and re-immersed immediately every minute. Under these conditions, approximately 3 µm of aluminium is removed from the surface.

After the etching, the cavities were cleaned using a standard solvent cleaning method. First they were rinsed by deionised water in a quick dump bath twice, then submerged first in acetone and subsequently in isopropanol, both for 5 minutes while subject to ultrasonic agitation, and lastly dried under a stream of nitrogen using a nitrogen gun.

3.4 Annealing

Another process investigated in connection with its effect on the quality factor of the superconducting resonators was annealing. In annealing, high temperatures are used to influence physical and/or chemical properties of a material. The process is used here in order to reduce the number of defects in the crystal lattice of the aluminium alloy.

The sample is heated above its recrystallization temperature, allowing for the migration of atoms in the crystal lattice and a subsequent reduction of defects. The process is thermodynamically favorable, as it leads to stress relief, but very slow at ambient temperature. However, the high-temperature enhanced diffusion can lead to a substantial decrease of the number of dislocations.

The cavities were annealed at 500 °C for 3 hours in a nitrogen atmosphere. The ramp up from room temperature to 500 °C, as well as the ramp down, was performed at a rate of 5 °C per minute.

3.5 Resonator measurements

In order to gather data necessary for the characterization of the resonant cavities, the cavities were mounted inside a dilution refrigerator in a reflection configuration. The measurement set-up is depicted in Figure 3.8.

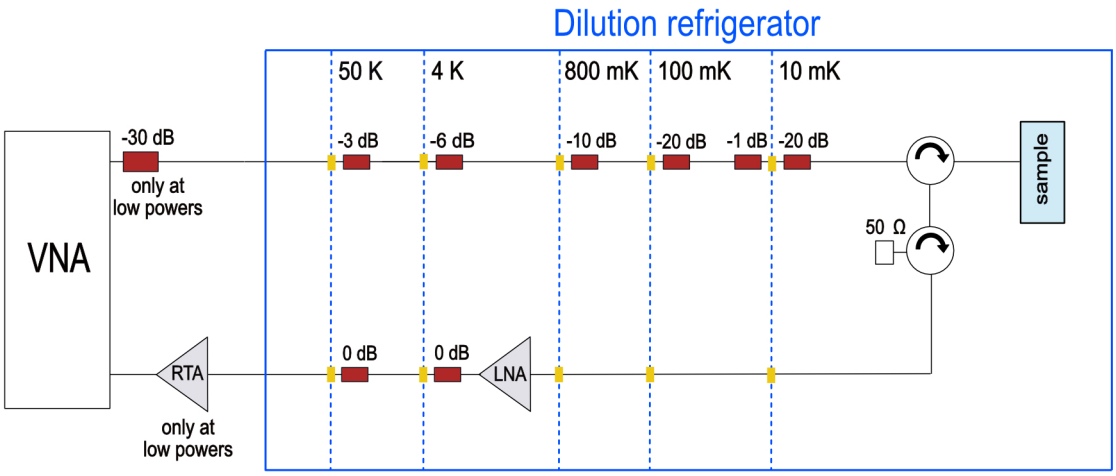

Figure 3.8: Resonator measurement set-up, displaying the vector network analyzer (VNA), room temperature amplifier (RTA), low-noise amplifier (LNA), various attenuators (represented by red rectangles), and the circulator-isolator unit.

3.5.1 Dilution refrigerator

A dilution cryostat is a cryogenic device that utilizes the thermodynamics of equilibrium disruption of a mixture of two helium isotopes, ^{3}He and ^{4}He, to reach and maintain milli-Kelvin temperatures. This mixture of ^{3}He and ^{4}He phase separates at 870 mK into a ^{4}He-rich phase, and a ^{3}He-rich phase that floats on top of the ^{4}He-rich phase. Removing ^{3}He from the dilute (^{4}He-rich) phase disturbs the thermodynamic equilibrium, and a fraction of the ^{3}He in the rich phase crosses the phase boundary to re-establish the disrupted equilibrium. This traversion of phase boundary is endothermic, resulting in further cooldown of the mixture.

As illustrated in Figure 3.8, the BlueFors LD50 dilution refrigerator used in these experiments has five stages thermalized to different temperatures, descending from top to bottom. Unless a temperature sweep was being performed, the temperature on the mixing chamber plate to which the samples were mounted was ≈10 mK. It can be noted that this is two orders of magnitude below the critical temperature T_c of aluminium, which is 1.2 K[27]. The reason behind going to such great lengths to achieve these temperatures is to mitigate noise produced by thermal fluctuations. As was mentioned in section 3.1, to operate a quantum circuit the system needs to be cooled to temperatures where the associated energy of thermal fluctuations k_BT is much lower than the transition energy $\hbar\omega_{01}$ between the two lowest energy levels of the system. A typical transition frequency of a superconducting qubit is in the 5-10 GHz range[6]. A frequency of 5 GHz corresponds to a temperature of about 240 mK, which is why superconducting circuits designed for quantum computation purposes are usually operated at milli-Kelvin temperatures.

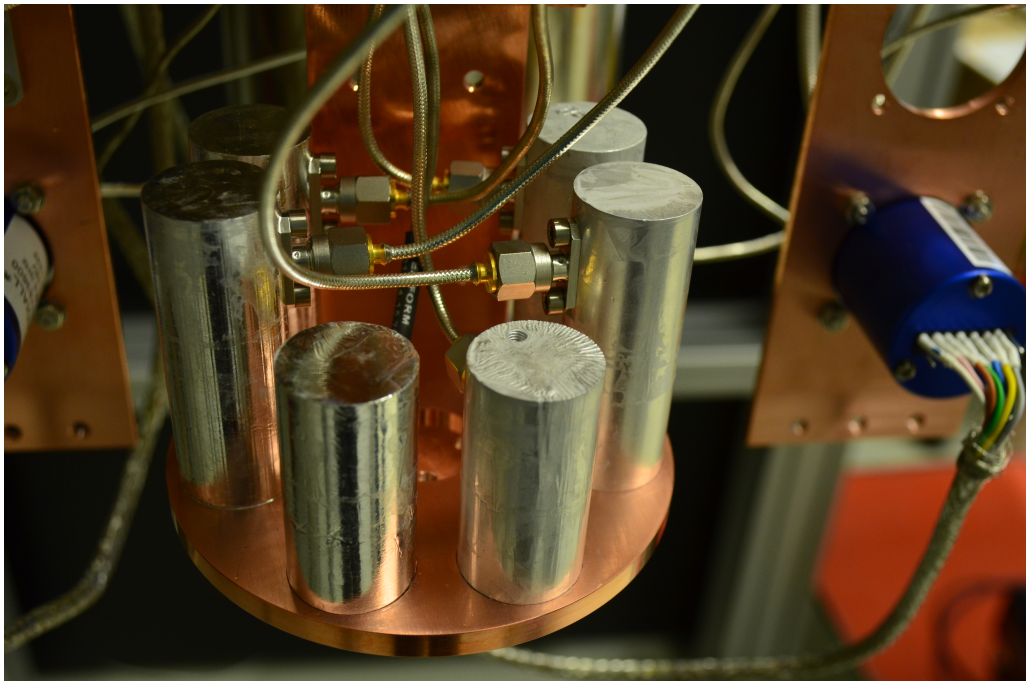

(a)

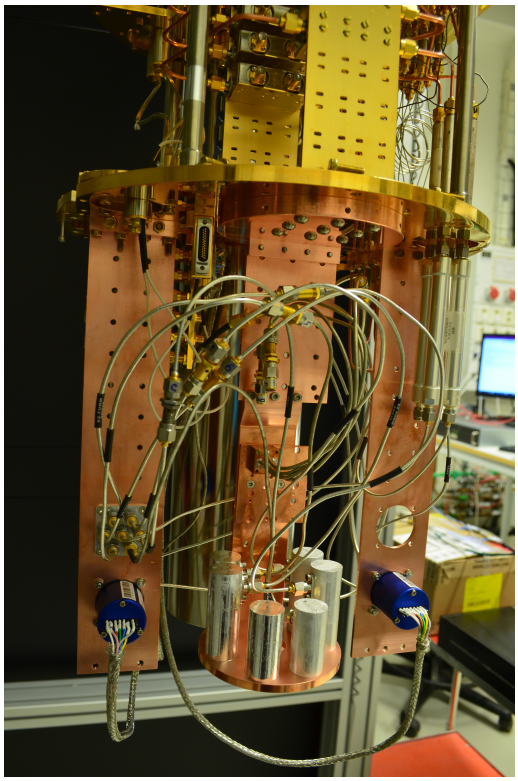

(b)

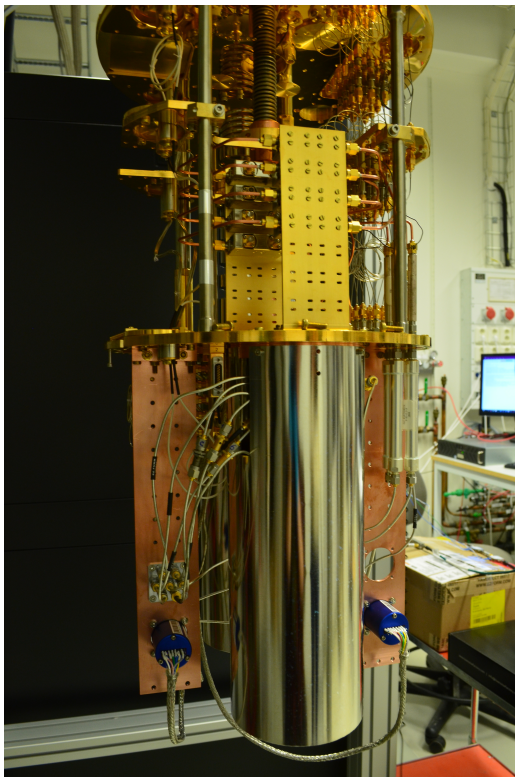

(c)

Figure 3.9: **(a)**, **(b)** Cavities are attached to a copper bracket with titanium screws. The bracket is mounted in the mixing chamber, which is below the lowest stage of the dilution refrigerator. **(c)** After the cavities are mounted, a Cryoperm magnetic shield is placed around the bracket. It should, however, be noted that magnetic cables were present inside the Cryoperm shield.

3.5.2 Scattering data measurement

The excitation signal for the microwave measurements of the cavities was generated in a vector network analyzer (VNA). A VNA is an instrument that can output continuous signals at frequencies inside a specified frequency window, and can record and analyze the amplitude and phase properties of the response.

The cavities were measured in a reflection configuration, as illustrated in Figure 3.8. The advantage of measuring resonance in reflection over transmission is that this way it is possible to directly determine the internal losses. In a transmission measurement where the resonance would appear as a peak in transmission, this is impossible due to the missing reference baseline[28]. To obtain the reflection coefficient in this set-up, the S_{21} scattering parameter was measured by the VNA using a circulator.

The VNA output signal was carried from room temperature to the mixing chamber of the dilution refrigerator via a coaxial transmission line. Inside the dilution refrigerator, the signal was attenuated at every stage with an overall attenuation summing up to 70 dB before reaching the samples. The purpose of these attenuators was thermal noise mitigation.

The cavity was connected to the circuit via a circulator-isolator unit. In this unit, two circulators are connected in series. The latter one termed 'isolator' is 50Ω-terminated at one port, allowing the signal to pass only one way.

The inbound microwave signal is sent to the sample through the first circulator. The signal reflected by the cavity is deflected by that same circulator towards the isolator. The signal passes through the isolator and continues its path towards the amplifier. Any signal reflected back (for example due to an impedance mismatch of microwave components on the output line) is deflected toward the 50 Ω-terminated port of the circulator and dissipated.

Power sweep

In the frequency spectrum of a resonator measured in reflection, a dip in the magnitude of the reflected signal appears at the frequency corresponding to the resonance frequency f_r, as shown in Figure 3.10 (a). The linewidth of the dip is inversely proportional to the quality factor of the resonator. The frequency spectrum can be measured with a VNA in a simple frequency sweep measurement.

After determining f_r from the frequency sweep, a power sweep was performed in a frequency window with f_r in the center at selected discrete VNA output powers. This was done in order to observe the dependence of the internal quality factor Q_i and the resonant frequency shift Δf_r on the driving power.

The power sweep was performed at $\approx 10\,\mathrm{mK}$ with VNA output powers ranging from -90 dBm to 12 dBm. The measurements were done in two rounds, a "high power" sweep and a "low power" sweep. The high power sweep was performed from 12 dBm to -60 dBm in 6 dBm increments with no added room temperature attenuation or amplification present. The low power sweep was performed from -18 to -90 dBm in 6 dB increments. A 30 dB attenuator was placed at the VNA output port during the low power sweep (as seen in Figure 3.8), converting the VNA output of 8 to -60 dBm to the desired -18 to -90. A room temperature amplifier was present

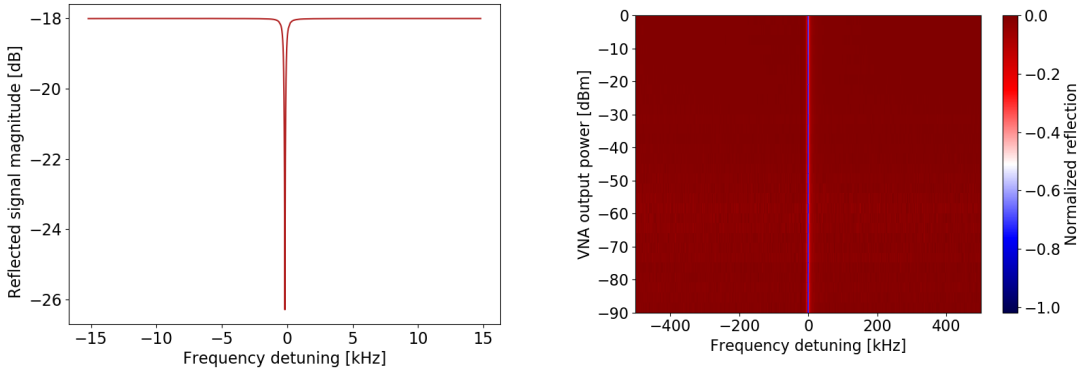

(a) **(b)**

Figure 3.10: **(a)** A dip in the magnitude of the reflected signal at the resonance frequency f_r **(b)** A power sweep on a selected frequency range.

on the VNA input line during the low power sweep.

Temperature sweep

To study the temperature dependence of the quality factor, the resonance of the cavity was probed at fixed powers while the temperature was increased from the base temperature of the mixing chamber from $\approx 10\,\text{mK}$ to $500\,\text{mK}$. The frequency window was identical to that probed during the previously performed power sweep. As before, the sweep was performed twice, in a "high power" and a "low power" round, using the same set-up with room temperature attenuators and amplifiers described in the previous section regarding power sweeps. For the high power temperature sweep, the VNA output power was 12 dBm, and for a low power sweep the output power was -50 dBm.

3.6 Scattering data analysis

A resonant circle fitting technique developed by Probst *et al.*[28] was used to analyze the scattering data gathered during the power and temperature sweeps. This fitting technique is a robust tool for analyzing complex scattering data on microwave resonators in the presence of noise. A demonstration of the fit is presented in Figure 3.11.

The total quality factor Q is denoted here as a "loaded" quality factor Q_l. Two loss paths are distinguished as contributions to a decrease in Q_l - the internal quality factor Q_i, and coupling (external) quality factor Q_c. These characterize the internal and external energy losses. Q_c is allowed to be complex valued here as $Q_c = |Q_c|e^{-i\phi}$, where the phase ϕ accounts for impedance mismatches. Q_l is then obtained by summing the reciprocal values of Q_i and the real part of Q_c:

$$\frac{1}{Q_l} = \frac{1}{Q_i} + \frac{1}{\mathbb{R}\{Q_c\}} \tag{3.4}$$

The reflection coefficient Γ was determined by measuring the complex scattering parameter S_{21} in reflection using a VNA, as described in the previous section. The reflection coefficient Γ can be expressed in terms of quality factors, taking the form:

$$\Gamma = ae^{i\alpha}e^{-2\pi f\tau}\left[\frac{2(Q_l/|Q_c|)e^{i\phi}}{1+2iQ_l(f/f_r-1)}-1\right] \tag{3.5}$$

where the terms in the square bracket represent the ideal resonator and the terms taken out in front represent the influence of the environment[28,29]. In this model, α is the phase shift, τ the electrical delay caused by the length of the cable, and a an additional amplitude to account for additional losses to and from the cavity. The fitting method estimates these parameters to normalize the data and then fits the resonance circle, which for the ideal resonator has a diameter of $d = Q_l/|Q_c|$.

From this, the loaded quality factor Q_l and the internal quality factor Q_i are determined. Q_i is of major interest here, as it quantifies the internal losses of the resonator. Q_c is adjustable by varying the length of the coupling pin, as described earlier in this chapter. To minimize the error of the fitting method, the coupling strength Q_c should be as close in value to Q_i as possible (close to the $Q_i = |Q_c|$ condition known as *critical coupling*), so the lengths of the coupling pins were often adjusted between cooldowns.

For a more intuitive reference, the input powers of the resonator excitations were converted to values corresponding to average photon numbers when plotting the power dependence of the quality factors:

$$< n >= \frac{4Q_l^2 P_{in}}{Q_c \hbar \omega^2} \tag{3.6}$$

where $< n >$ is the average photon number in the cavity at an input power P_{in}.

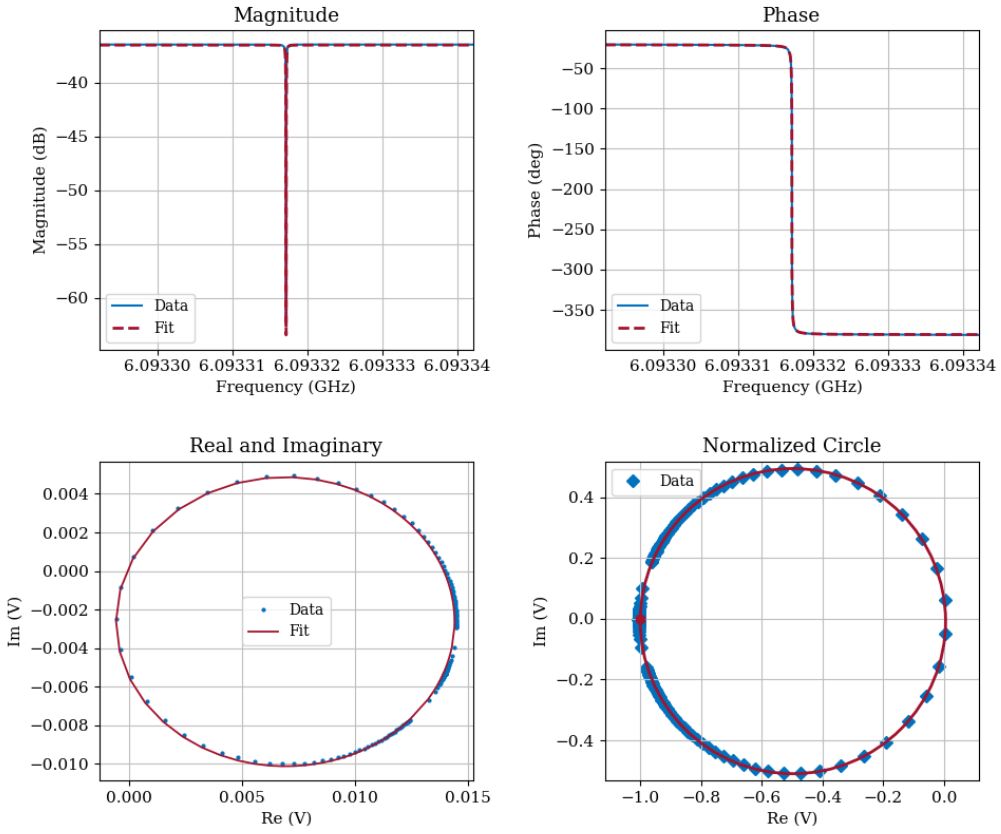

Figure 3.11: A demonstration of the resonance circle fit of the scattering data gathered during a frequency sweep performed at a fixed power. In a $\lambda/4$ resonator, a dip in the magnitude response and a shift in the phase response is expected at resonance[30]. A fit of the amplitude and phase response data is shown in the top left and top right, respectively. The fit of the resonant circle obtained by plotting the real and imaginary parts of the S_{21} parameter measured in reflection is demonstrated in the two bottom plots. The measured data was normalized in the fit to restrict the diameter of the resonant unit circle, as shown in the bottom right plot.

4

Results

4.1 Electropolishing of flat testpieces

4.1.1 Linear sweep voltammetry

At first, linear sweep voltammetry (LSV) measurements were performed at 30 °C. The individual sweeps were carried out at different sweep rates between voltages ranging from the open circuit voltage E_{OC} to 30 V, which was the maximum voltage output of the potentiostat used in these experiments. The results of these measurements are presented in Figure 4.1.

An interesting feature can be observed in this figure - the first measurement trace taken has a different trend compared to the subsequent ones, even compared to a trace taken at the exact same sweep rate (20 mV/s). This effect was observed in later experiments as well, and after some observation it was possible to trace it down to the value of E_{OC}. Every sweep was initiated after E_{OC} stabilized - however, the potential had a tendency to stabilize around two different values: $-1.67\,\mathrm{V}$ or $-1.22\,\mathrm{V}$. Before every first measurement initiated after the immersion of a sample into the electrolyte, E_{OC} corresponded to around $-1.67\,\mathrm{V}$. After a measurement was done, E_{OC} always stabilized around $-1.22\,\mathrm{V}$. However, if the waiting time before external voltage was applied again was long enough (on the order of 3-5 minutes), E_{OC} started to drop and stabilized again around $-1.67\,\mathrm{V}$ again. It was observed that whenever an LSV sweep was initiated at the E_{OC} of $-1.67\,\mathrm{V}$, the trace resembled the first one taken in this measurement. After this observation, measurements initiated at the same E_{OC} were found reproducible.

This effect could be explained by the formation of a viscous diffusion layer at the surface of the working electrode. It is possible that some time at an applied voltage is necessary for the film to be formed properly so that the polishing can be realized in a controlled manner. If the external voltage is switched off, the film is slowly reduced to an ordinary diffusion film corresponding to the dynamic equilibrium between the solution and the surface of the workpiece, and the layer characteristic for the electropolishing process is lost. Since this observation, all LSV experiments on the flat testpieces were performed with an initial voltage sweep that served to bring the system into the desired state with an E_{OC} of $-1.22\,\mathrm{V}$. This first trace was disregarded in further data analysis. After the initial sweep, measurements were started immediately after E_{OC} stabilized around $-1.22\,\mathrm{V}$. When initiated at the same starting conditions, the measurement traces were reproducible.

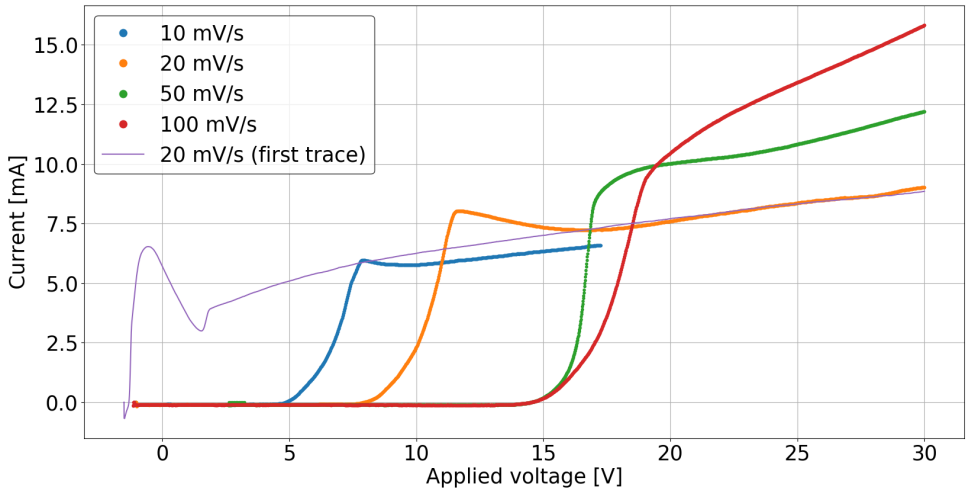

Figure 4.1: LSV at 30 °C for different sweep rates. Measured currents are plotted against the voltage applied between the working and the counter electrode.

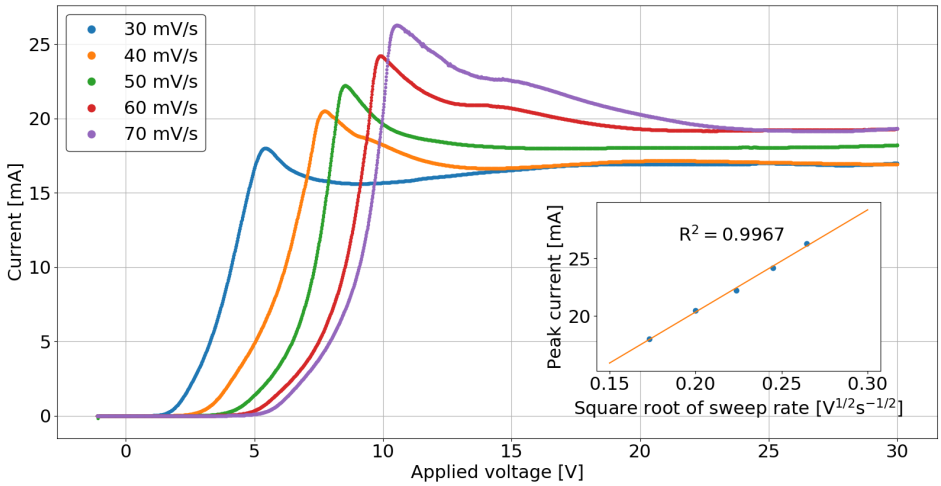

Figure 4.2: LSV of the same sample as in Figure 4.1 after the temperature of the electrolyte was raised to 50 °C. The inset shows a linear fit of the peak currents vs. square roots of scan rates. The linear fit extrapolates to the origin, and the coefficient of determination of the fit is $R^2 = 0.9967$.

Moving to the remaining traces, it can be observed that the peaks and plateaus that would indicate the presence of the limited current regime during the LSV do not appear at higher sweep rates at all. At lower sweep rates peaks are present, but are not well pronounced. Thus, it cannot be reliably stated that a diffusion-limited anodic brightening regime had been reached in this experiment.

As the diffusion-limited regime was not observed at 30 °C, the electrolyte still containing the same sample was heated up to 50 °C and measured again in a similar

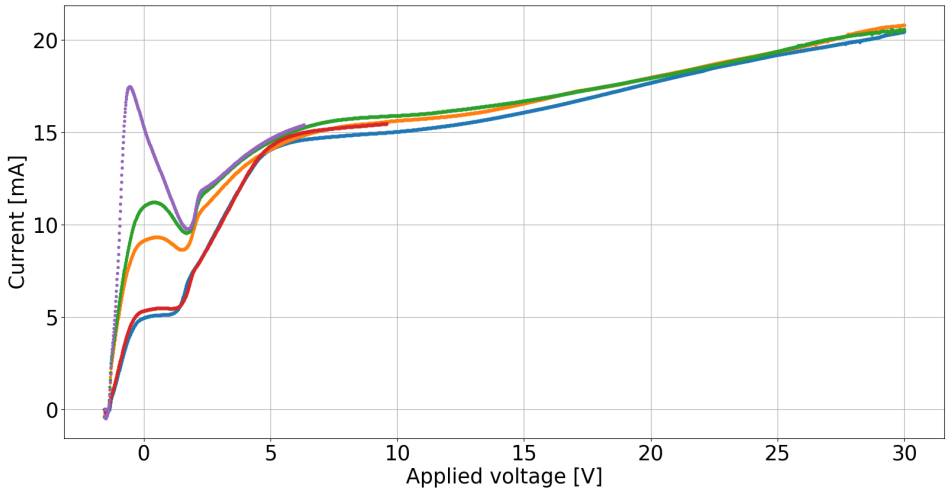

Figure 4.3: LSV performed on a sample put directly into a 50 °C electrolyte without keeping it at a lower temperature beforehand. All traces were taken at a sweep rate of 50 mV/s.

fashion. This time, distinct peaks and plateaus were observed in the polarization curves in Figure 4.2. The dependence of the peak currents on the square root of the scan rates is decidedly linear, which adds further weight to the claim that diffusion-limited regime has indeed been reached during the sweeps.[22,31]

After this experiment, another sample was immersed directly into a 50 °C electrolyte and LSV measurements were performed in order to check the reproducibility of the previously obtained results. This time, however, the results defied expectations, as can be observed in Figure 4.3. Even after several sweeps were performed, E_{OC} always stabilized around −1.67 V, and none of the traces taken in these measurements showed signs of the previously obtained polarization curve. Instead, the curves resembled the other traces taken in previous experiments at an E_{OC} of −1.67 V, peaking around the region where the applied voltage changed signs. All the traces in Figure 4.3 were performed at a sweep rate of 50 mV/s to observe the shift of the polarization curve in the voltage spectrum. Interestingly enough, even though the LSV was performed repeatedly at the same sweeping rate, the peak currents around 0 V rose with the consecutive traces.

To see whether the fact that the samples stayed in 30 °C acid for some time before the temperature was raised to 50 °C made a difference, or whether it was the effect of the sweeps done at the temperature, two experiments were made. First, the procedure leading to the results in Figures 4.1 and 4.2 was reproduced - the sample was first put into 30 °C acid and the same voltage sweeps were made in the same order as on the previous sample, and then the temperature was raised to 50 °C and the sweeps presented in Figure 4.4 were made. In the other experiment, a new sample was immersed in a 30 °C electrolyte for 1.5 hours, which was approximately the time that the sweeps performed on the first sample at 30 °C took, but no external voltage was applied on the electrodes. Afterwards, the sweeps shown in figure 4.5 were performed.

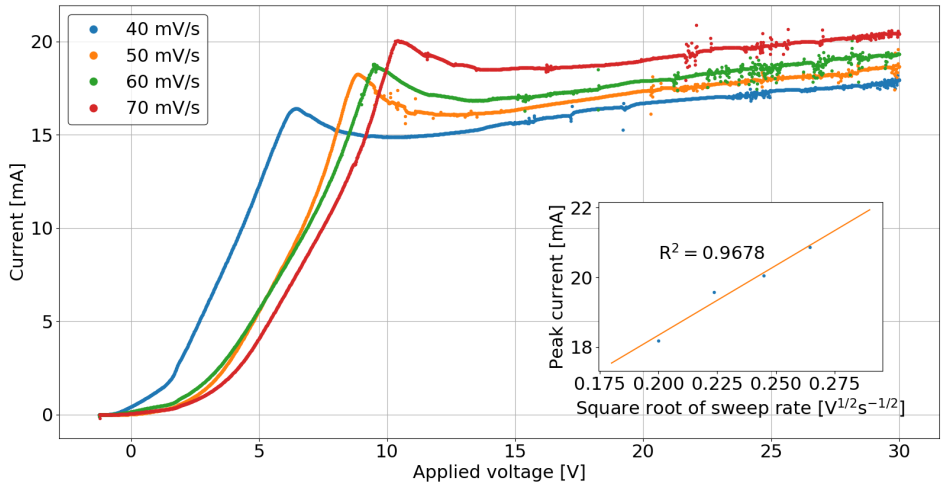

Figure 4.4: LSV at 50 °C after sweeps were performed at 30 °C.

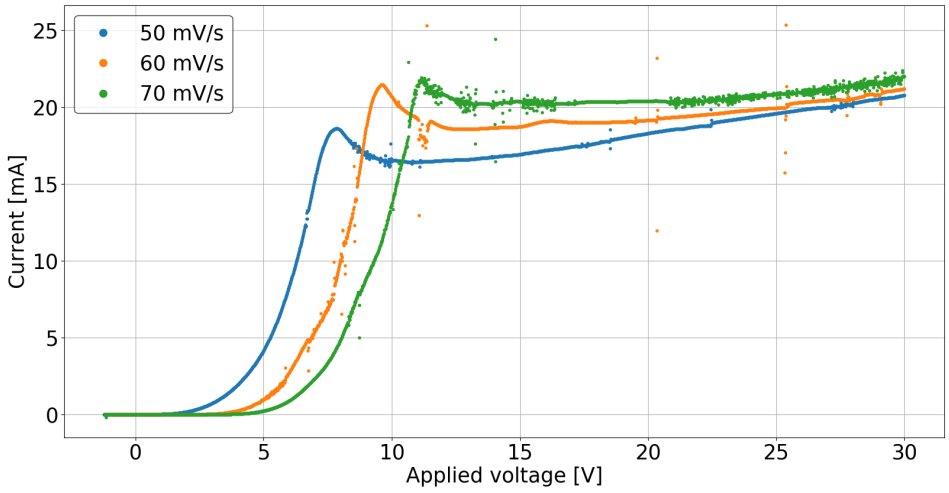

Figure 4.5: LSV at 50 °C after the sample had been left to etch in the electrolyte bath at 30 °C for 1.5 hours.

Both results indicate that the micropolishing regime had been reached, regardless of whether external voltage was applied on the electrodes during the time the sample was immersed in the 30 °C acid. A possible explanation would be that the process, being rather complex, is very sensitive to the state of the surface. It is possible that when the aluminium sample was exposed to atmosphere, organic molecules and other impurities present in air deposited on the surface. Exposure to atmospheric humidity and oxygen could have affected the native oxide layer present on the aluminium surface as well. This could then influence the formation of the viscous layer between the anode and the electrolyte, preventing the process from reaching the diffusion-limited anodic brightening regime. The deposited impurities would, however, be

etched away by the concentrated acids if left immersed for a certain time, restoring the aluminium surface.

4.1.2 Combining LSV with chronoamperometry

As it was clear that the sweep rate has an effect on the position of the different polishing regimes in the voltage spectrum, presumably by the way of influencing the properties of the viscous film surrounding the working electrode, the next test was to establish whether the speed with which the constant voltages are reached influence the final steady state at that voltage. For this purpose the idea was to combine LSV with chronoamperometry (CA). A voltage was picked from the beginning of the limiting current plateaus (13V) and an LSV sweep was performed at different rates until that voltage was reached. Once 13V were reached, the voltage was kept constant for 15 minutes while the current passing between the electrodes was recorded.

An LSV sweep at 50 mV/s was performed directly before the start of these measurements with notice of the E_{OC} taken. In figure 4.6 it can be observed that even though the final polishing voltage was reached with different speeds, the final steady state current at 13 V was the same for all three measurements, presumably characteristic for the voltage in this system.

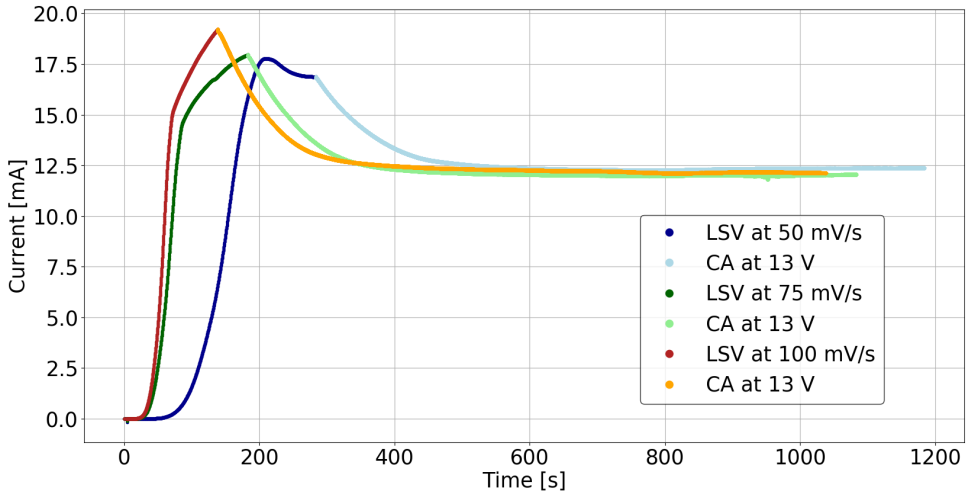

Figure 4.6: LSV at three different sweep rates until 13V with subsequent chronoamperometry (CA) at 13 V for 15 minutes.

4.1.3 Chronopotentiometry

The next step was to see the behaviour of the system at a constant current, while the potential of the working electrode measured against the SCE reference was measured over time. While for simple systems it should make no difference whether it is the current or the voltage that is controlled, for more complex systems this need not be true. Since the electrochemistry of aluminium is indeed complex, the current

corresponding to the steady state current reached at 13 V (12 mA) was selected and the attempt at a chronopotentiometry measurement lasting 20 minutes was made. As can be seen in Figure 4.7, this particular measurement was cut off after little more than 9 minutes when the rising voltage crossed 30 V, which is the maximum voltage supported by the potentiostat used to perform these measurements. Because of this, lower currents were chosen in the next CA measurements, but the voltage did not always stabilize, nor were the results reproducible. It should also be noted that these currents are much lower than any of the currents of the limiting plateaus measured with LSV, which might be the answer to why no satisfactory results were obtained.

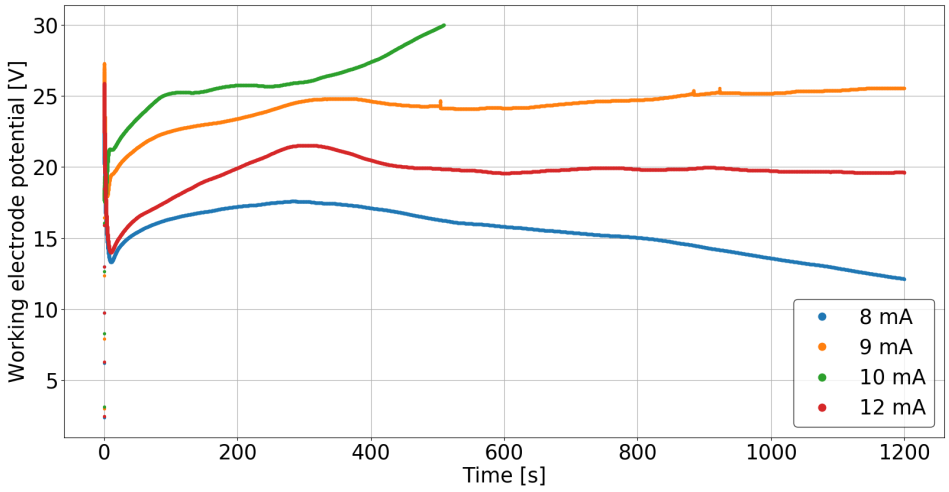

Figure 4.7: Chronopotentiometry for 4 different currents selected from the vicinity of the steady state current at 13V. The potential of the working electrode is measured in reference to a saturated calomel reference electrode.

4.1.4 Chronoamperometry

After the brief excursion into the world of chronopotentiometry, the return to chronoamperometry was made. The samples were to be polished at three different applied voltages - the previously applied 13V from the beginning of the plateau, and then 25V and 30V that still lie on the limiting plateau. In the first run, the samples were polished at a given constant voltage for 40 minutes. With these samples it was clear to the naked eye that the polishing had not been sufficient, as the scratches on the surface and the milling marks left from the machining were still visible. The samples were observed under a Dektak surface profiler to ascertain whether any of the voltages were favorable. The traces taken over a 500 µm length can be seen in Figure 4.9. To compare, a trace taken over the same length span on an unpolished sample is plotted in Figure 4.8.

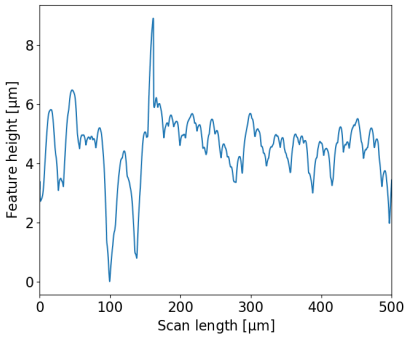

Figure 4.8: Surface profiler trace taken over a 500 µm length on an unpolished sample.

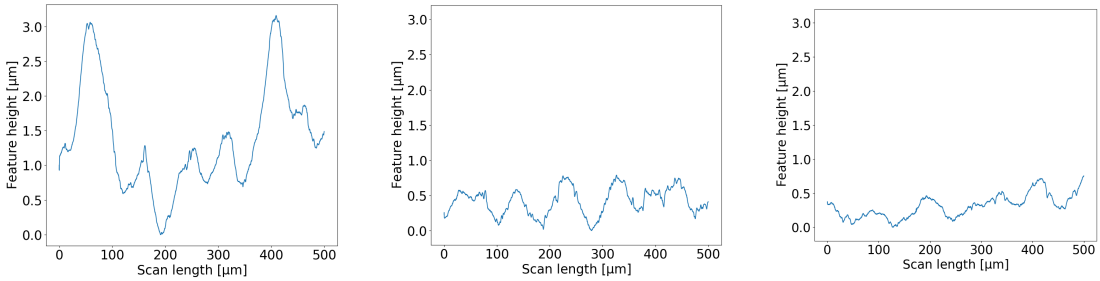

(a) **(b)** **(c)**

Figure 4.9: Surface profiler trace taken over a 500 µm length after the samples were polished for 40 minutes at a) 13 V, b) 25 V and c) 30 V.

Judging by the results of the surface profiler, it can be observed that that 13V had not produced the best results, seeing that the features were on the order of several µm. Polishing at a higher voltage gave much better results, thus the following experiments were performed only with 25 and 30V. There is a possibility that at 13 V the system was not truly operating in the diffusion-limited regime, seeing as 13 V was right at the beginning of the plateau in the polarization curves taken at lower sweeping rates, but at higher rates the plateau was not truly there yet.

As the results were not quite satisfactory yet, electropolishing time was increased to 1 hour and 20 minutes. When the polished samples were taken out of the electrolyte, the scratches and milling marks were not visible anymore, but another problem presented itself - it would appear that during the polishing the oxygen evolution became quite substantial, producing bubbles which subsequently by sitting on the surface of the sample presented a barrier between the electrolyte and the surface and left craters in their wake.The surface traces taken with a surface profiler are presented in Figure 4.10. The resulting features were several µm high, so there conditions were not fit either.

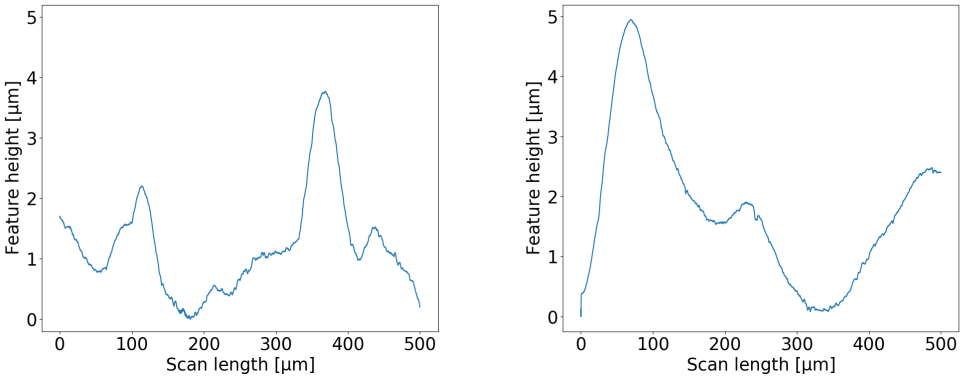

(a) **(b)**

Figure 4.10: Surface profiler trace taken over a 500 µm length after the samples were polished for 1h 20 minutes at a) 25 V and b) 30 V.

After the observation that longer polishing times produced bubble marks, the next polishing experiment was done in shorter cycles. The cycles were 20 minutes long and at the end of each the sample was taken out of the electrolyte, rinsed thoroughly in deionized water, dried under a stream of nitrogen gas and put back into the vessel for another cycle. Some bubble marks still appeared on the surface, but were less pronounced than in the previous experiment. The surface traces taken with a surface profiler are presented in Figure 4.11.

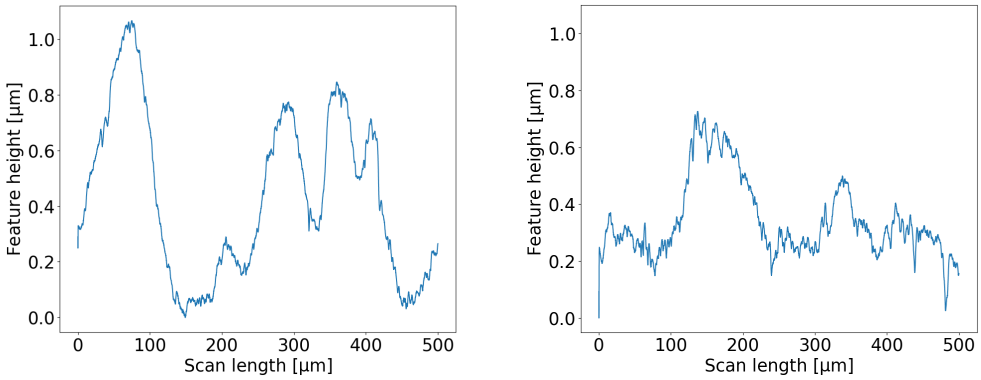

(a) **(b)**

Figure 4.11: Surface profiler trace taken over a 500 µm length after the samples were polished for 1h 20 minutes in 20-minute cycles at a) 25 V and b) 30 V.

Higher voltages were investigated in further experiments. Since the potentiostat used in the previous experiments had a maximum voltage output of 30 V, a voltage source with the maximum output of 60 V was used. Cycles of 20 minutes were investigated at 40 V, 50 V and 60 V. At first the polished samples looked very smooth to the naked eye with very little bubble markings visible, but when inspected 24 hours after the polishing, it was observed that the surface had turned entirely

white. This indicates that the surface had not passivated under the electropolishing conditions and was later covered with a thick layer of aluminium oxide on contact with air. Since this is undesirable, these voltages were not investigated further.

Ultrasonic agitation was proposed as a means of mitigating the effect caused by the oxygen bubble evolution. However, electropolishing under ultrasonic agitation at various powers resulted in samples that appeared highly reflective, but had macroscopic features resembling "shelves" of flat, reflective surfaces several hundreds of micrometers in size. A rise in current was also observed when the ultrasonic agitation was turned on. This was attributed to the ultrasonic agitation disturbing the diffusion layer, and this method of agitation was not used in further experiments.

4.2 6081 aluminium alloy cavities

Before undergoing any electrochemical procedure, the cavities were treated by annealing and etching at various temperatures and times, and were measured in a dilution cryostat following to every treatment. These experiments were performed by Marina Kudra at the Quantum Technology Laboratory of the Department of Microtechnology and nanoscience, Chalmers University of Technology.

As was established by studying the electrochemical behaviour of the flat testpieces, all electrochemical procedures were initiated by first sweeping the voltage at 30 °C until the resulting polarization curves achieved reproducibility, and only then the temperature was raised to the desired LSV or electropolishing temperature. During the temperature ramp-up from 30 °C, voltage sweeps were performed in order to prevent chemical etching in the absence of external potential.

For the 6081 alloy cavities, a changed in the color of the electrolyte was observed during LSV or chronoamperometry at higher temperature (50 °C). This color change occurred gradually from the initial transparent state of the electrolyte towards a dark grey color in a span of approximately 1.5-2 hours, depending on the electrochemical procedure. This color change is captured in Figure 4.12). No color change of the acid was perceptible at 30 °C.

4.2.1 Short 6081 cavity

A summary of the treatment that the short 6081 alloy cavity underwent before any electropolishing procedures, as well as the f_r and Q_i measured after each of the previous treatments, can be found in Table 4.1.

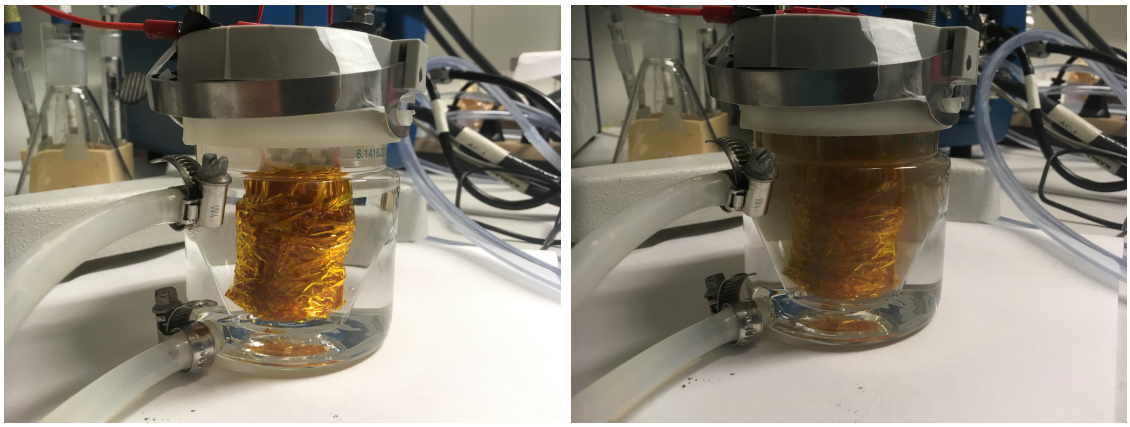

(a) **(b)**

Figure 4.12: The color change of the electrolyte from the initial transparent state right after the immersion of the 6081 aluminium alloy cavity **(a)** to a dark gray color after the electropolishing process **(b)**

Treatment				Result	
Step	Type	Temperature	Time	f_r [GHz]	Q_i [10^6]
1	as machined	—	—	5.99756	4
2	annealing	300 °C	2 hours	5.99682	3.9
3	annealing	500 °C	3 hours	5.99601	7.8
4	etching	RT	20 minutes	5.99551	1.5
5	etching	50 °C + RT	4 hours + 20 minutes	5.97560	5.85

Table 4.1: Q_i and f_r values after different treatments of the short 6081 Al cavity

LSV

After initial sweeps at 30 °C performed until the traces became reproducible, signaling the stabilization of the temperature of the electrolyte as well as the diffusion layer, the temperature of the electrolyte was raised to 50 °C.

At 50 °C, LSV traces were taken at a sweep rate of 50 mV/s. This sweep rate was chosen as a compromise between slower sweeps that were rejected in order to minimize time spent in the etching regime, and faster sweeps where the polishing plateau had a tendency to become less distinct in non-ideal conditions (as demonstrated by the LSV measurements performed at 30 °C on the flat testpieces shown in Figure 4.1).

In the LSV traces taken at 50 °C with a sweep rate of 50 mV/s, presented in Figure 4.13, a feature resembling a plateau can be observed before the peak of the polarization curve is reached. This feature is not unique to this particular cavity, but appeared in other samples as well. At first it was attributed to a copper leak into the electrolyte, or impurities in the 6081 alloy. However, the feature remained in later experiments where no evidence of a copper leak was present, as well as when

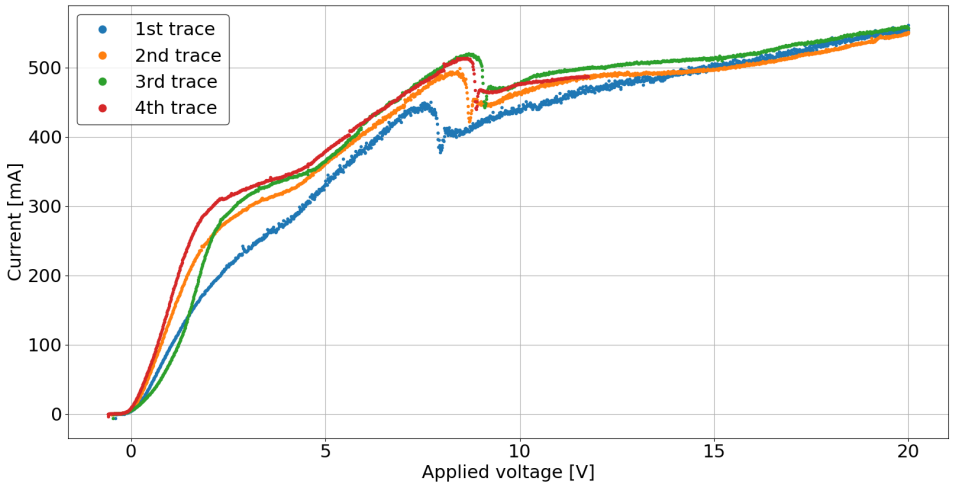

Figure 4.13: LSV traces of the short 6081 aluminium cavity, taken at 50 °C at a sweep rate of 50 mV/s.

copper tape was replaced by aluminium tape. This behaviour was also present in the polarization curves of the 4N aluminium cavities. Thus, it appears that this behaviour is characteristic of this system, and the two features diverging from the exponential increase of current with driving force are evidences of two different rate-limiting mechanisms.

From Figure 4.13 it can also be observed that with successive traces, the "second plateau" had a tendency to shift towards higher voltages and currents at first before stabilizing. After the position of the plateau became reproducible, LSV measurements were interrupted and the electropolishing phase was initiated. Based on the polarization curve in Figure 4.13, a constant potential of 9 V was selected for the chronoamperometric stage.

Electropolishing

To ensure that the electropolishing was indeed performed in the limited current regime, chronoamperometry was preceded by a voltage sweep while the current was monitored, and only after that the cavity was electropolished at a constant voltage. For the short 6081 cavity, the voltage picked from the previously taken LSV traces was 9 V. Based on the experiments with flat testpieces, the constant voltage was held for 20 minutes before the next round was allowed to start from the E_{oc} or the point of observable chemical etching. For the short 6081 cavity this process was repeated 3 times. Since this was the first cavity to undergo this procedure,

The current recorded during the LSV and the subsequent chronoamperometry is plotted in Figure 4.14. It can be observed that the polarization curve, as well as the current passing between the electrodes at constant applied voltage, was consistent between the cycles.

In Figure 4.14 it can be observed that when the voltage sweep was switched into the constant voltage mode, the flowing electric current dropped at first before

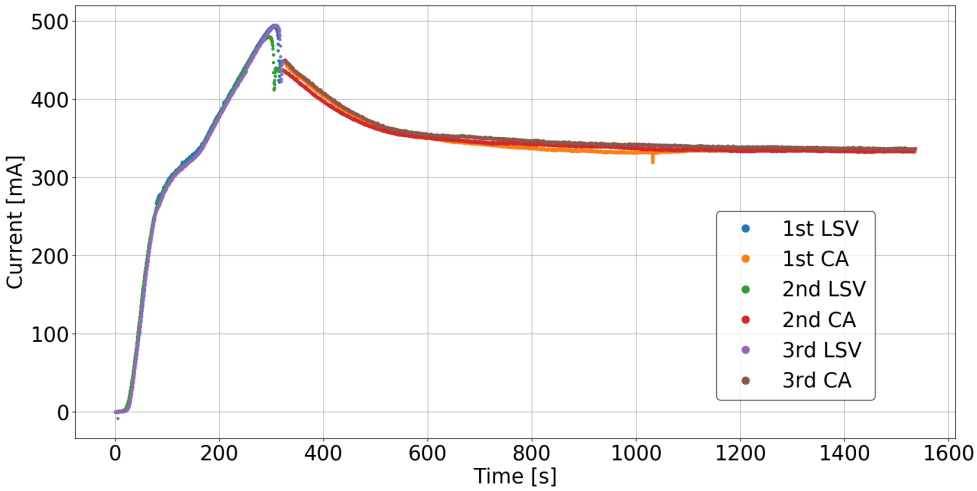

Figure 4.14: Electropolishing of the short 6081 cavity, performed at 50 °C. LSV at 50 mV/s is terminated and followed by chronoamperometry (CA) at 9 V. The constant voltage of 9 V is held for 20 minutes during CA.

stabilizing at a lower value. This effect was expected. The total current measured by the potentiostat has both faradaic contributions resulting from the redox reactions at the electrodes, and non-faradaic contributions. During a voltage sweep, the electrode acts like a capacitor as well, and a charging current develops through the cavity as long as the applied voltage keeps changing. When the applied voltage is kept constant, the charging current ceases to contribute, and the measured current flow is lower than that measured during a voltage sweep.

A change of appearance of the aluminium cavity surface after electropolishing is shown in Figure 4.15. A mitigation of surface roughness on the order of the visible light scattering can be observed in the increased reflection of the center post.

Microwave measurements

The Q factors extracted from power sweep measurements performed in a dilution refrigerator at ≈10 mK before and after the electropolishing are plotted in Figure 4.16. The green dashed line indicates the probe power corresponding to a single photon in the cavity.

The measurements show that the internal quality factor of the resonator approximately doubled as an effect of electropolishing from the initial value of 5.85×10^6 to 11.5×10^6. The resonance frequency of the cavity after electropolishing was 5.990 56 GHz.

An interesting result is the increase of power dependence of the Q_i of the electropolished cavity as opposed to the cavity before electropolishing. This hints at an increase in the dominance of TLS losses in the overall internal loss for the polished cavity.

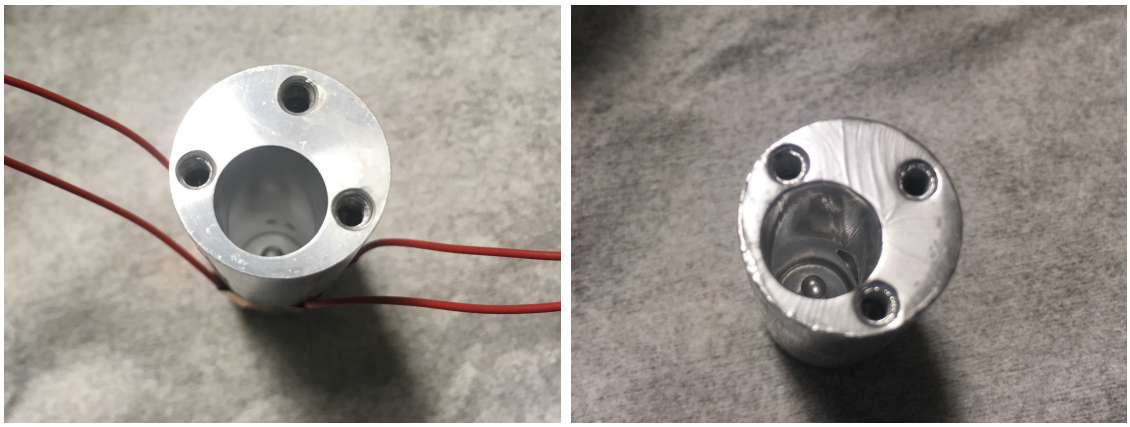

(a) **(b)**

Figure 4.15: A picture of the short 6081 aluminium cavity before **(a)** and after **(b)** electropolishing.

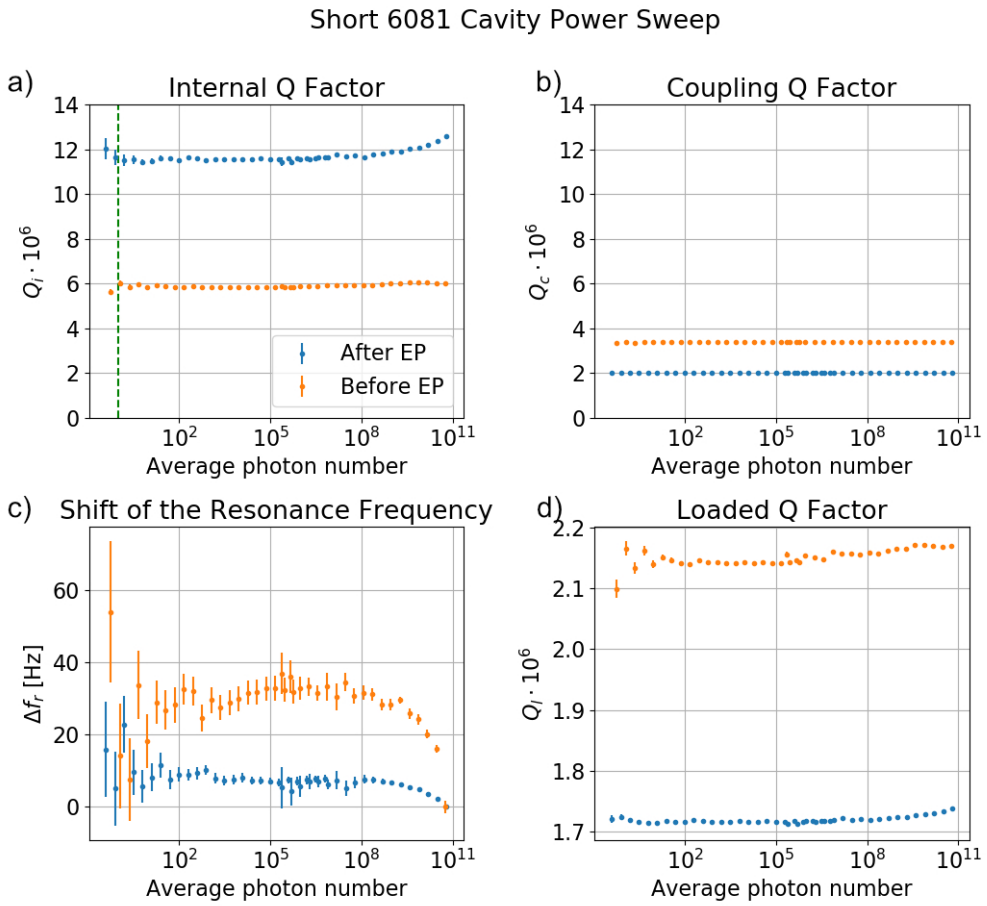

Figure 4.16: Power sweep of the short 6081 aluminium alloy cavity before and after electropolishing (EP), displaying the increase of Q_i from a low-power value of 5.85×10^6 before EP to 11.5×10^6 after EP. **a)** shows the power dependence of Q_i with the green vertical line indicating the single-photon energy level, **b)** the power dependence of Q_c, **c)** the resonance frequency shift compared to the resonance frequency at the highest power measured, and **d)** the power dependence of Q_l.

4.2.2 Long 6081 cavity

A summary of the different treatments of the long 6081 alloy cavity is listed in Table 4.2.

Treatment				Result	
Step	Type	Temperature	Time	f_r [GHz]	Q_i [10^6]
1	as machined	—	—	5.96352	4
2	etching	50 °C	4 hours	5.93092	4
3	etching	RT	20 minutes	5.93077	4.3
4	annealing	500 °C	3 hours	5.92868	12.9

Table 4.2: Q_i and f_r values after different treatments of the long 6081 Al cavity

Electropolishing

As previously, LSV measurements were performed at 30 °C and 50 °C. This time, however, the traces taken at 50 °C showed no tendency repeating current values, but instead kept increasing slightly with every subsequent trace. The previous behavior of the plateau to shift towards higher values and later become reproducible was, however, retained, and the electropolishing was initiated upon this stabilization. Six polishing cycles were performed on the long cavity, as this proved beneficial in the flat testpieces. The last cycle was interrupted after approximately eight minutes, as the electrolytic solution reached a dark gray color.

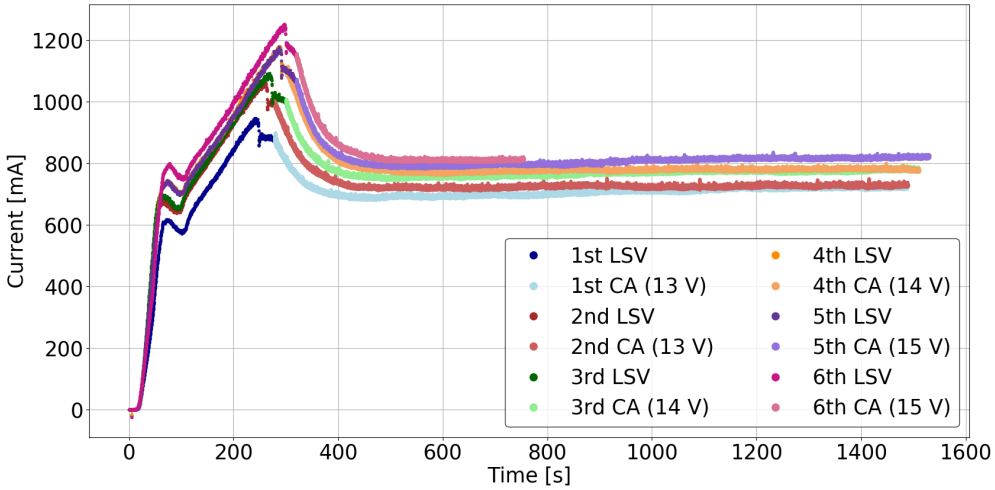

Figure 4.17: Electropolishing of the long 6081 cavity, performed at 50 °C. LSV at 50 mV/s is terminated and followed by chronoamperometry (CA) at voltages indicated in the legend. The constant voltage is held for 20 minutes during CA apart from the last CA, which was terminated after 8 minutes.

After removing the outside protection of the cavity, a suspicion that the acid breached the coating and attacked the copper tape arose. To alleviate this, the

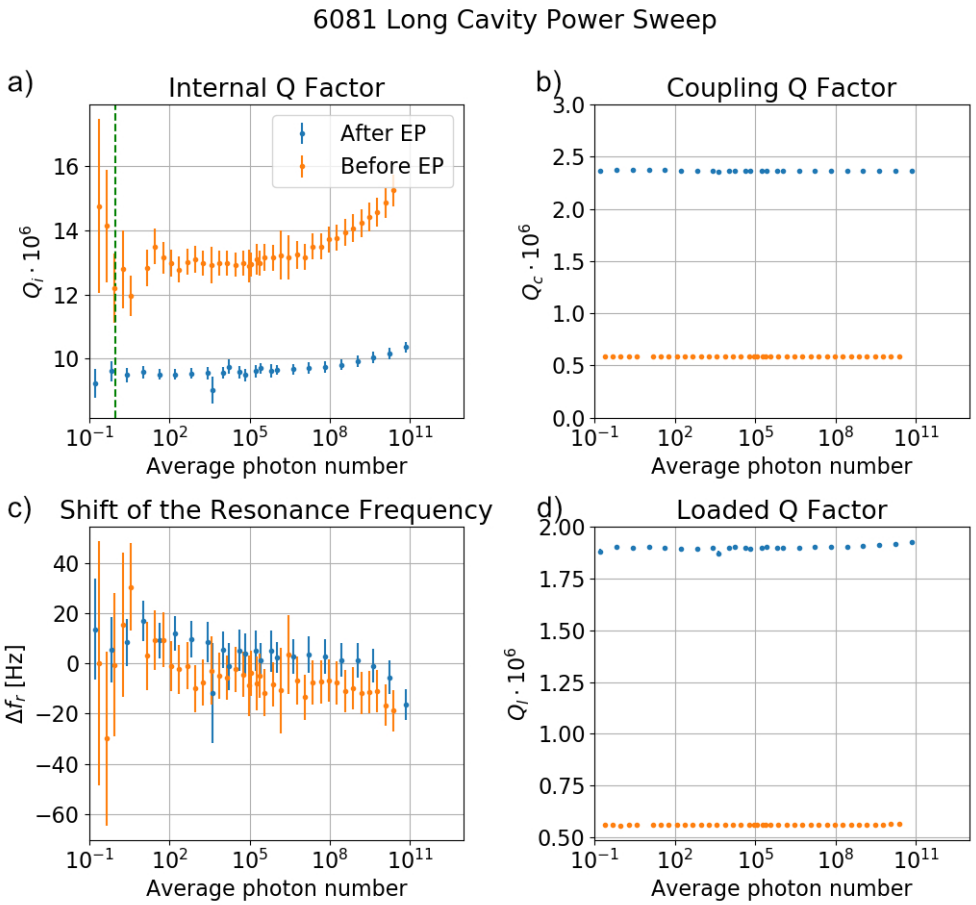

Figure 4.18: Power sweep of the long 6081 aluminium alloy cavity before and after electropolishing (EP), displaying the decrease of Q_i from a low-power value of 12.9×10^6 before EP to 9.9×10^6 after EP. **a)** shows the power dependence of Q_i with the green vertical line indicating the single-photon energy level, **b)** the power dependence of Q_c, **c)** the resonance frequency shift compared to the resonance frequency at the lowest power measured, and **d)** the power dependence of Q_l.

cavity was etched with room temperature aluminium etchant for five minutes before being solvent cleaned inside a clean room facility.

Microwave measurements

The results of the subsequent low temperature measurements are presented in Figure 4.18. It can be observed that this time, the electropolishing had an adverse effect on the internal quality factor of the resonator. After electropolishing, the Q_i of the cavity dropped from the previously measured low-power value of 12.9×10^6 to 9.9×10^6. This time, an increase of power dependence compared to the previous measurement of the unpolished cavity was not observed. The resonance frequency of the cavity after the electropolishing treatment was 5.898 35 GHz.

There are various possible reasons for this decrease in Q_i. Some of them might be related to the geometry of the set-up. As seen in Figure 4.12, the long cavity

takes up the majority of the space in the vessel, and the level of acid over the top of the workpiece is around 1 cm. This restricts the flow of the electrolyte significantly, especially bearing in mind the long and narrow geometry of the cavity. The cavity sites considered most crucial in terms of electropolishing of the resonant cavities are the top of the center pin and its surroundings, all located in the lower part of the cavity where the acid flow is extremely restricted. This could lead to limited extraction of the reaction products from the aluminium surface, and even saturation of the acid located in the bottom of the cavity, unable to flow out. In the upper parts of the cavity the flow was aided by the vigorous hydrogen evolution at the graphite electrode, but the bottom sections lacked this agitation. The electropolishing procedure relies on shifting the chemical equilibrium and controlling the rates of the occurring reactions. A scenario where, for example, the phosphoric acid saturates and no longer assists in removing aluminium oxide from the cavity surface, is a situation hardly beneficial for performing measurements based on superconductivity.

Another aspect to consider here is that the electropolishing plateau appeared at higher voltages here than in the short 6081 cavity. It has been demonstrated in the experiments done on flat testpieces that higher voltages lead to oxygen evolution that leaves marks on the aluminium surface.

For further investigation of the process, the polishing could be performed in a larger vessel allowing for electrolyte flow, or a polishing procedure at a lower applied voltage could be attempted. Annealing of the cavity after electropolishing could also be investigated, as it could improve the uniformity of the oxide. If the decrease in Q_i was an effect of oxidation, annealing the cavity could be benificial in this case.

4.3 4N aluminium cavities

The same experimental protocol of sweeping the voltage at 30 °C to the point of reproducibility before raising the temperature further was followed for the 4N (99.99% pure Al) cavities as for the 6081 ones. This time, however, a difficulty in establishing the polishing plateau was observed at 50 °C, and the temperature was raised further to 60 °C. At 60 °C the system was still very sensitive and hard to stabilize, but it was possible to reach a limited current plateau.

As opposed to the treatment of the 6081 alloy, the 4N aluminium did not discolour the electrolytic solution.

4.3.1 Short 4N cavity

Before being electropolished, the short 4N cavity underwent the treatment summarized alongside the resulting f_r and low-power Q_i in Table 4.3.

LSV

As before, the cavity was immersed in a 30 °C solution and 50 mV/s voltage sweeps were performed while current was recorded. These measurements are shown in Figure 4.19. An interesting trend is shown here, where each following trace displays lower and lower currents. At first, the current drop is more significant, later becomes

Treatment				Result	
Step	Type	Temperature	Time	f_r [GHz]	Q_i [10^6]
1	as machined	—	—	5.98164	4.3
2	annealing	300 °C	2 hours	5.98095	4.4
3	annealing	500 °C	3 hours	5.98094	4.4
4	etching	RT	20 minutes	5.98020	11.8
5	etching	50 °C + RT	4 hours + 20 minutes	5.93193	27.9
6	annealing	500 °C	3 hours	5.93193	29.0

Table 4.3: Step by step treatment of the short 4N cavity before electropolishing, with the Q_i and f_r values measured after each treatment.

milder, and finally the traces start overlapping. This could signify the decrease of oxidizable material on the surface, be it the decrease of surface area as a result of mitigated surface roughness, or the removal of aluminium compounds and impurities.

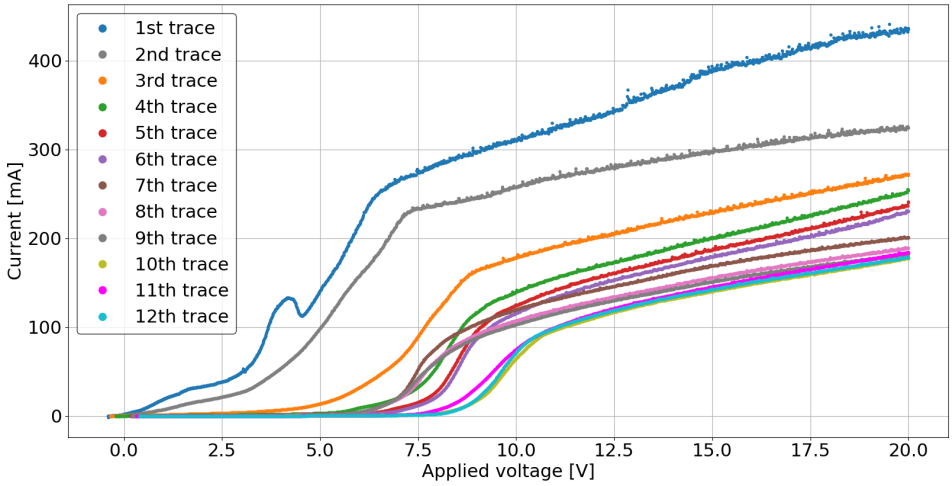

Figure 4.19: LSV of the short 4N cavity at 30 °C. All the traces are performed at a sweep rate of 50 mV.

Next, the temperature of the electrolyte was raised to 60 °C while voltage sweeps were performed continuously to mitigate chemical etching. Monitoring the current during these sweeps brings an interesting insight into the properties of the electropolishing system. It appears that with rising temperature, the passing current also increases (see Figure 4.20). This is consistent with previous measurements on flat testpieces that showed higher currents at 50 °C than at 30 °C. From this it can be concluded that an increase in temperature has a positive effect on the redox reaction rate.

After the temperature of the electrolyte reached 60 °C, more LSV measurements

were taken at 50 mV/s, shown in Figure 4.21. Again the initial drop of high voltage currents with consecutive traces can be observed before this trend is reversed. In the low voltage part of the spectrum it can be seen that the current peaks needed some time before being able to form, and more to become pronounced. This could be a feature of the system, or a sign that the cavity needed more time to reach a thermal equilibrium with the newly heated electrolyte, especially as the cavity was insulated from the outside with various materials, and the majority of the exposed surface was a part of a narrow geometry with little hydrodynamic agitation.

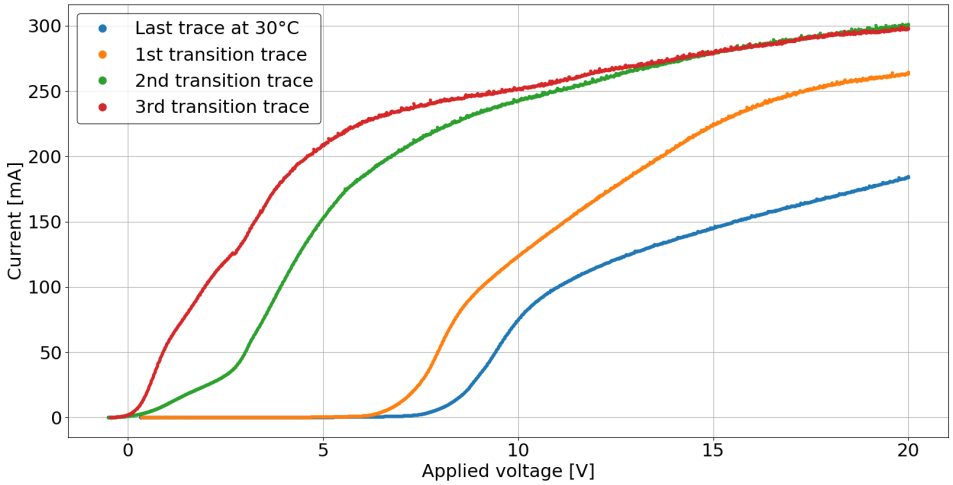

Figure 4.20: LSV of the short 4N cavity, performed during a temperature ramp-up from 30 °C to 60 °C. All traces are taken at a sweep rate of 50 mV/s.

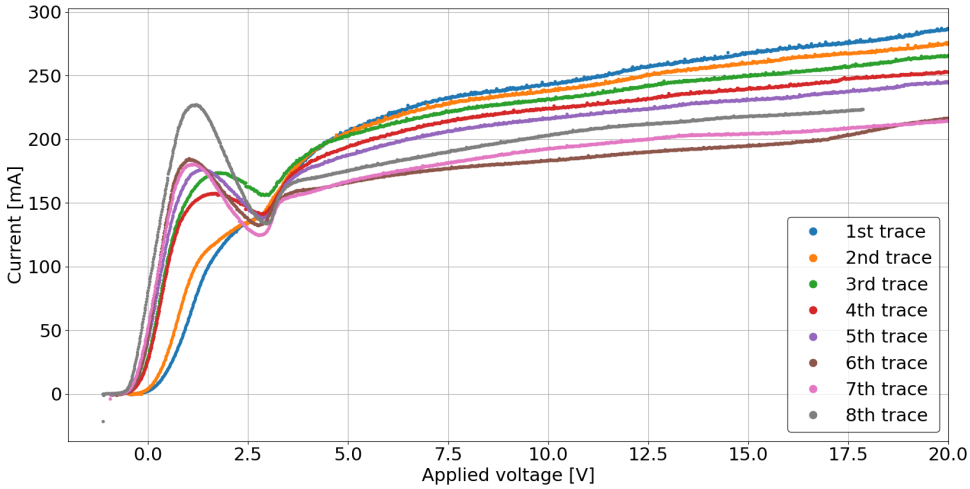

Figure 4.21: LSV of the short 4N cavity at 60 °C. All the traces are performed at a sweep rate of 50 mV.

Electropolishing

After the LSV measurements, the cavity was taken out of the electrolyte, rinsed in deionized water and dried under a stream of nitrogen gas to restore the surface and prevent pitting as a result of prolong exposure to acids.

Afterwards, the cavity was put back into the vessel along with a fresh electrolyte, and again LSV was performed at 30 °C until the point of reproducibility, followed by a raise to 60 °C. However, this time sweeps at 60 °C were performed only until they started developing a plateau, not until they became reproducible. The concern behind this decision was that losing too much material in the high-temperature polishing would lead to the thinning of the wall between the cavity and the screw threads, and eventually towards the removal of that wall. This would mean that the cavity could no longer be mounted into the dilution refrigerator for microwave measurements.

A voltage of 6 V was selected from the LSV performed at 50 mV/s. Figure 4.22 shows fluctuations in the current peaks during the earlier sweeps, and stabilization in later ones. The plateaus had a tendency to shift in voltage, which was accounted for in subsequent sweeps by changing the value of the constant voltage. After the end of each sweep the voltage was kept constant for 20 minutes, except for the first run where the CA was interrupted after approximately 7.5 minutes due to the irregularities in the current peak preceding the CA.

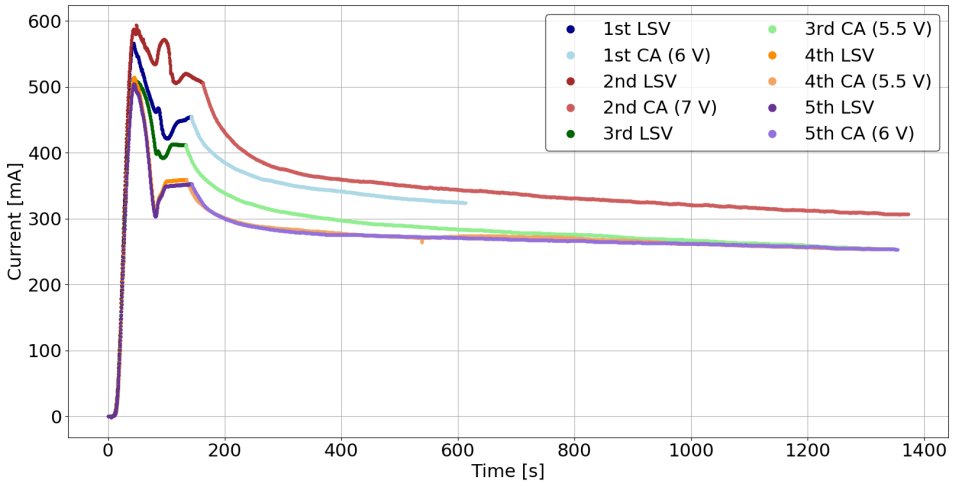

Figure 4.22: Electropolishing of the short 4N cavity at 60 °C, performed by sweeping up to a selected voltage (indicated in the legend) with a sweep rate of 50 mV/s, and keeping that voltage constant for 20 minutes in a chronoamperometry (CA) measurement. The second CA performed was interrupted after 7.5 minutes.

Microwave measurements

After this treatment, the cavity was solvent cleaned and stored in a nitrogen box inside a cleanroom facility until the time of mounting inside a dilution refrigerator.

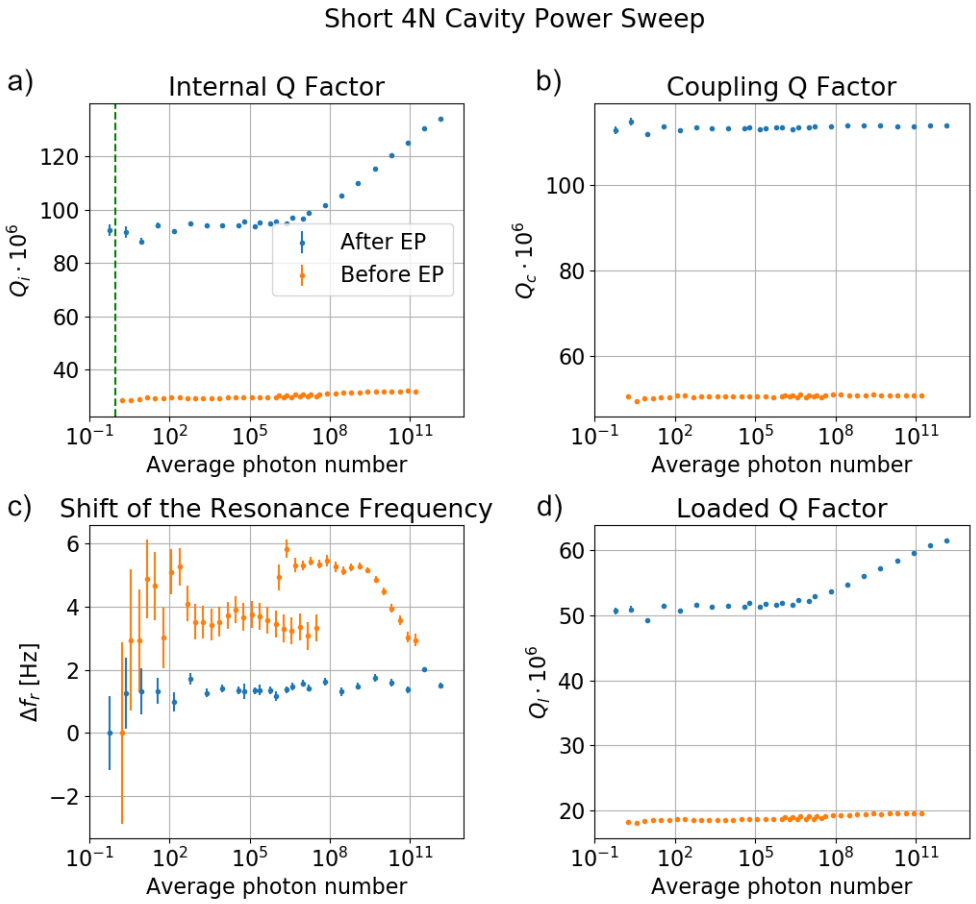

Figure 4.23: Power sweep of the short 4N aluminium cavity before and after electropolishing (EP), displaying the increase of Q_i from a low-power value of 29×10^6 before EP to 94×10^6 after EP. **a)** shows the power dependence of Q_i with the green vertical line indicating the single-photon energy level, **b)** the power dependence of Q_c, **c)** the resonance frequency shift compared to the resonance frequency at the lowest power measured, and **d)** the power dependence of Q_l.

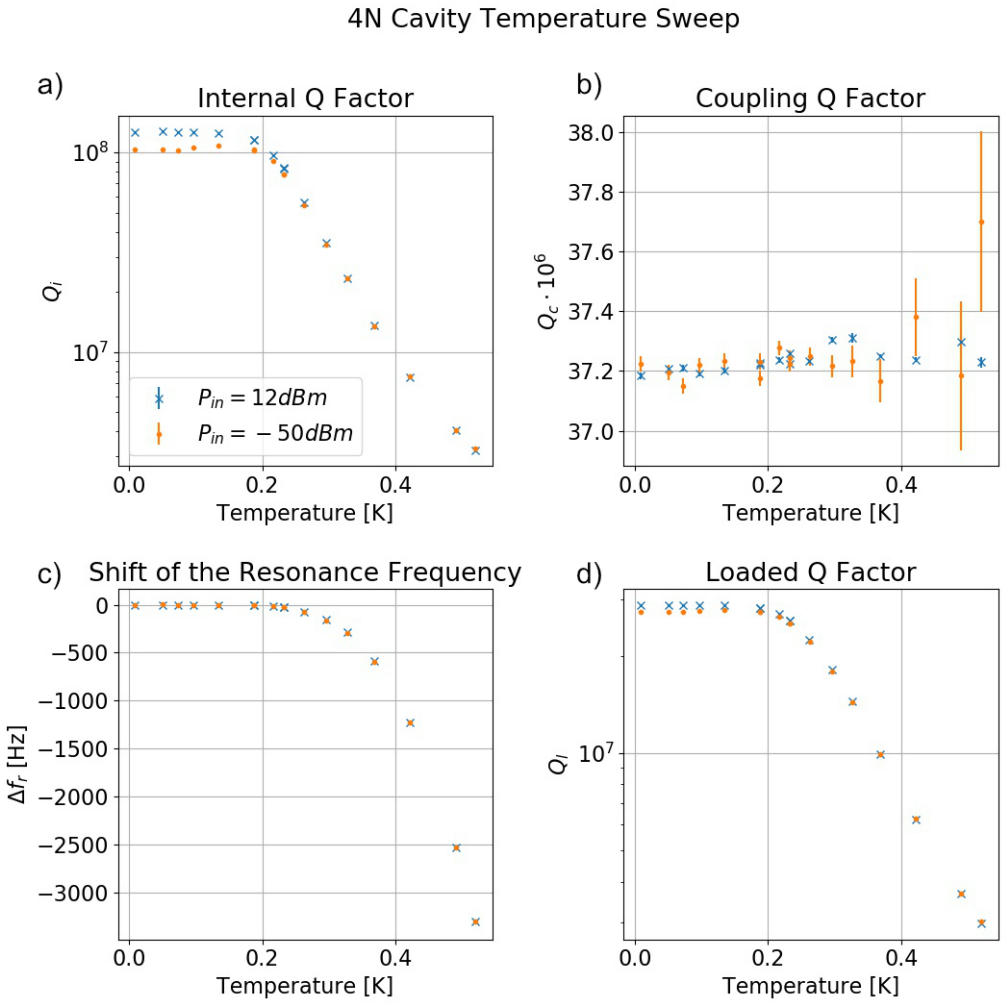

Figure 4.24: Temperature sweep of the short 4N aluminium cavity at two different fixed probe powers. Here we observe Q_i values above 10^8 until 200 mK and a sharp decline in Q_i at higher temperatures. **a)** shows the temperature dependence of Q_i, **b)** the temperature dependence of Q_c, **c)** the resonance frequency shift compared to the resonance frequency at the temperature measured, and **d)** the temperature dependence of Q_l.

The cavity was measured during two separate cooldowns in the same dilution refrigerator, the second time with coupling adjusted to approach critical coupling. The results of both measurements were comparable. Results of the power and temperature sweeps of the second measurements are shown in Figure 4.23 and 4.24. The power sweep in Figure 4.23 was performed in the second cooldown with adjusted coupling, the temperature sweep in 4.24 in the first cooldown when the cavity was over-coupled to a coupling quality factor Q_c of 37×10^6.

As both short cavities had not been able to reach Q_i as high as the long cavities despite having received the same treatment, the conclusion that these cavities were limited by seem loss due to their length had been reached. However, the results of the power sweep in Figure 4.23 indicate otherwise, showing a tripling of the Q_i after electropolishing from the initial low-power value of 29×10^6 to 94×10^6, the highest value reached in this work.

The Q_i after electropolishing shows an increased power dependence as well. This is usually a sign of TLS loss and is most likely coming from the surface oxide.

The resonance frequency f_r of the electropolished cavity was 6.093 32 GHz, as opposed to 5.931 93 GHz before electropolishing. This increase in resonance frequency is not unexpected, as the removal of the cavity surface altered the dimensions of the waveguide.

The temperature sweep of the cavity shows that the Q_i and f_r of the cavity are stable until 200 mK. A decrease in Q_i and a shift in f_r is observed afterwards. This behaviour is expected and is a result of thermal excitations leading to an increase in quasiparticle density.

4.3.2 Long 4N cavity

The different treatments of the long 4N aluminium cavity before electropolishing are summarized in the table below:

Treatment				Result	
Step	Type	Temperature	Time	f_r [GHz]	Q_i [10^6]
1	as machined	—	—	9.96599	8.2
2	annealing	500 °C	hours	5.96529	9.5
3	etching	RT	20 minutes	5.96594	15.2
4	etching	50 °C	4 hours	5.92801	67
5	annealing	500 °C	3 hours	5.92800	77

Table 4.4: Q_i and f_r values after different treatments of the long 4N Al cavity before electropolishing.

Electropolishing

The current measurement taken during the electropolishing preceded by LSV performed at 30 °C and 60 °C can be seen in Figure 4.25. The polishing was performed at 60 °C by sweeping with 50 mV/s until 7 V, which was then kept constant for 20 minutes. This was repeated 5 times, with every following trace reaching lower currents. The cavity appeared highly reflective after the electropolishing process,

with little to no visible markings and a clear reflection of the center post and the cavity walls.

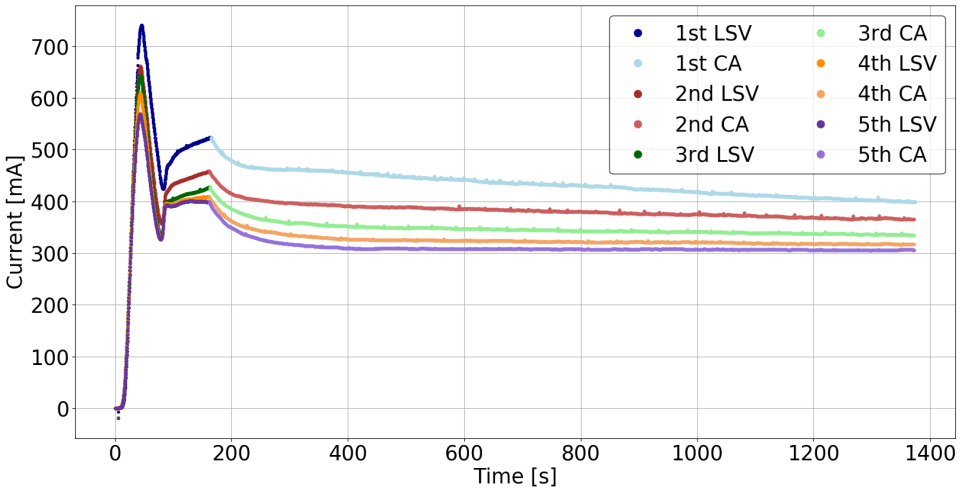

Figure 4.25: Electropolishing of the long 4N aluminium cavity by sweeping the applied voltage with a rate of 50 mV/s until 7V and keeping the voltage constant for 20 minutes.

Microwave measurements

Despite the high reflectivity of the cavity surface, the Q_i measured during the subsequent power sweep showed a considerable drop from the previously measured low-power value from 77×10^6 to 25×10^6, which is a significant drop in quality.

The power dependence of the electropolished cavity is much stronger compared to the previous measurement. This hints at the previously reached conclusion that for electropolishing long cavities in this set-up, oxidation of the aluminium surface poses a risk. To investigate this, the cavities could be annealed and measured again.

Another reason for this drop in Q_i might be that during the electropolishing and the preceding LSV measurements, so much material was removed that the properties of the waveguide had changed, shifting the field distribution in the cavity and rendering the geometry of the waveguide less than optimal. As before, the resonance frequency f_r shifted, this time from 5.928 00 GHz to 5.994 54 GHz. This reflects the alteration of the cavity dimensions.

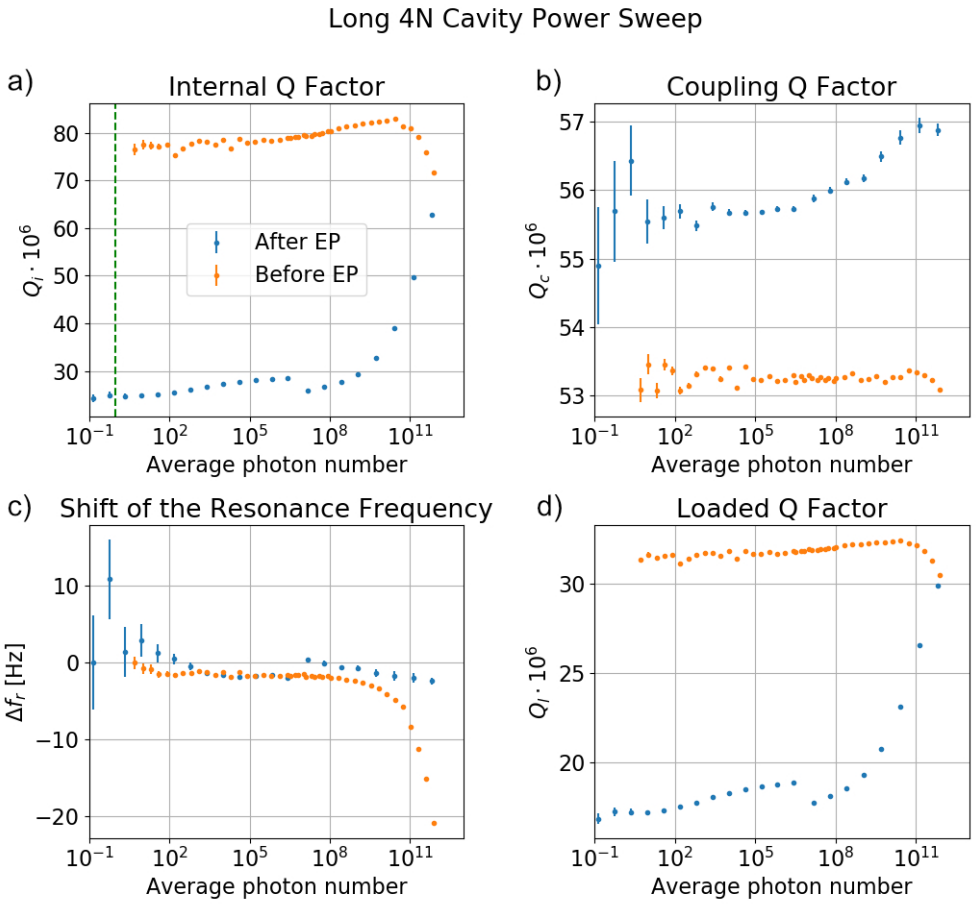

Figure 4.26: Power sweep of the long 4N aluminium cavity before and after electropolishing (EP), displaying the decrease of Q_i from a low-power value of 77×10^6 before EP to 25×10^6 after EP. **a)** shows the power dependence of Q_i with the green vertical line indicating the single-photon energy level, **b)** the power dependence of Q_c, **c)** the resonance frequency shift compared to the resonance frequency at the lowest power measured, and **d)** the power dependence of Q_l.

5
Conclusion

Electropolishing of the superconducting aluminium cavity surface was found to have a high impact on the resulting internal quality factor of the resonant cavities measured at millikelvin temperatures.

Cavities of two different lengths, 35 mm and 50 mm, were investigated in this work. Cavities of both lengths were fabricated from a 6081 alloy with a 96.3-98.6% aluminium content, and a 4N alloy with a 99.99% aluminium content.

In the process implemented in this work, shorter cavities of both aluminium grades were shown to improve with electropolishing, whereas the Q_i of the longer cavities decreased. Cavities of both lengths fabricated from the 4N alloy showed higher values of Q_i than cavities fabricated from the 6081 alloy. A summary of the results is listed in Table 5.1.

For short cavities, the increase in low-power Q_i after electropolishing was from 5.85×10^6 to 11.5×10^6 for the 6081 alloy, and from 29×10^6 to 94×10^6 for the 4N aluminium. In a temperature sweep performed on the short 4N cavity, Q_i was stable until 200 mK and decreased sharply at higher temperatures as a result of thermal excitations. Both short cavities displayed an increase of the power dependence of Q_i after electropolishing, which hints at an increased dominance of the TLS loss path to the overall energy loss. The increase in Q_i could then be explained as a mitigation of resistive loss at the cavity surface by decreasing the specific surface of the cavity.

For long cavities, the decrease in low-power Q_i after electropolishing was from 12.9×10^6 to 9.9×10^6 for the 6081 alloy, and from 77×10^6 to 25×10^6 for the 4N aluminium. The decrease in Q_i upon electropolishing might be due to the constrained geometry of the electropolishing set-up, which did not allow for electrolyte flow in the lower sections of the cavity, thus hindering the reaction products from diffusing away from the surface, shifting the electrochemical equilibrium, and disturbing the electropolishing process.

Material	Length	Q_i [10^6]	
		Before EP	After EP
6081	35 mm	5.85	11.5
	50 mm	12.9	9.9
4N	35 mm	29	94
	50 mm	77	25

Table 5.1: Internal quality factors of the cavities before and after electropolishing (EP).

Bibliography

[1] R. Feynman, "Simulating physics with computers", *International Journal of Theoretical Physics*, vol. 21, pp. 467–488, 1982.

[2] M. Nielsen and I. Chuang, *Quantum Computation and Quantum Information*. Cambridge University Press, 2010, ISBN: 978-1-10700-217-3.

[3] M. Reagor, H. Paik, G. Catelani, L. Sun, C. Axline, E. Holland, I. M. Pop, N. A. Masluk, T. Brecht, L. Frunzio, M. H. Devoret, L. Glazman, and R. J. Schoelkopf, "Reaching 10 ms single photon lifetimes for superconducting aluminum cavities", *Applied Physics Letters*, vol. 102, p. 192 604, 2013.

[4] C. C. Gerry and P. L. Knight, "Quantum superpositions and Schrödinger cat states in quantum optics", *American Journal of Physics*, no. 65, pp. 964–974, 1997.

[5] A. Romanenko and D. Schuster, "Understanding quality factor degradation in superconducting niobium cavities at low microwave field amplitudes", *Physical Review Letters*, vol. 26, no. 119, 2017.

[6] M. H. Devoret and J. M. Martinis, "Implementing qubits with superconducting integrated circuits", *Quantum Information Processing*, vol. 3, pp. 163–203, 2004.

[7] M. Tinkham, *Introduction to superconductivity*, 2nd ed. Dover Publications, 2004, ISBN: 0-486-43503-2.

[8] R. Feynman, *The Feynman Lectures on Physics*, 3rd ed. Basic Books, 2010, vol. 3, ISBN: 978-0-465-02501-5.

[9] S. M. Girvin, "Circuit QED: Superconducting qubits coupled to microwave photons", *Lecture Notes of the Les Houches Summer School*, vol. 96, pp. 1–155, 2011.

[10] A. Megrant, C. Neill, R. Barends, B. Chiaro, Y. Chen, L. Feigl, J. Kelly, E. Lucero, M. Mariantoni, P. J. J. O'Malley, D. Sank, A. Vainsencher, J. Wenner, T. C. White, Y. Yin, J. Zhao, C. J. Palmstrøm, J. M. Martinis, and A. N. Cleland, "Planar superconducting resonators with internal quality factors above one million", *Applied Physics Letters*, vol. 100, p. 113 510, 2012.

[11] D. Niepce, *Nanowire superinductors*, Licenciate thesis, Chalmers University of Technology, 2018.

[12] A. D. O'Connell, M. Ansmann, R. C. Bialczak, M. Hofheinz, N. Katz, E. Lucero, C. McKenney, M. Neeley, H. Wang, E. M. Weig, A. N. Cleland, and J. M. Martinis, "Microwave dielectric loss at single photon energies and millikelvin temperatures", *Applied Physics Letters*, vol. 92, p. 112 903, 2008.

[13] P. Macha, S. H. W. van der Ploeg, G. Oelsner, E. Il'ichev, H.-G. Meyer, S. Wünsch, and M. Siegel, "Losses in coplanar waveguide resonators at millikelvin temperatures", *Applied Physics Letters*, vol. 96, p. 062 503, 2010.

[14] T. Brecht, M. Reagor, Y. Chu, W. Pfaff, C. Wang, L. Frunzio, M. H. Devoret, and R. J. Schoelkopf, "Demonstration of superconducting micromachined cavities", *Applied Physics Letters*, vol. 107, no. 19, 2015.

[15] M. J. Reagor, "Superconducting cavities for circuit quantum electrodynamics", PhD thesis, Yale University, 2015.

[16] C. Hamann, A. Hamnett, and W. Vielstich, *Electrochemistry*, 2nd ed. Wiley-VCH, 2007, ISBN: 978-3-527-31069-2.

[17] G. Yang, B. Wang, K. Tawfiq, H. Wei, S. Zhou, and G. Chen, "Electropolishing of surfaces: Theory and applications", *Surface Engineering*, vol. 33, pp. 149–166, 2017.

[18] C. Strong, "Faraday's laws in one equation", *Journal of Chemical Education*, vol. 31, p. 226, 2013.

[19] F. M. Abouzeid and H. Abubshait, "A study of vitamin B influence on the morphology, roughness, and reflectance of electropolished aluminum in H_3PO_4-H_2SO_4 mixture", *Arabian Journal of Chemistry*, 2018.

[20] D. Landolt, "Fundamental aspects of electropolishing", *Electrochimica Acta*, vol. 32, pp. 1–11, 1987.

[21] S. Van Gils, S. Holten, E. Stijns, M. Vancaldenhoven, H. Terryn, and L. Mattsson, "Electropolishing of aluminium: Processing and assessment of visual appearance", *Surface and Interface Analysis*, vol. 35, pp. 121–127, 2003.

[22] M. Haidopoulos, S. Turgeon, C. Sarra-Bournet, G. Laroche, and D. Mantovani, "Development of an optimized electrochemical process for subsequent coating of 316 l stainless steel for stent applications", *Journal of Materials Science: Materials in Medicine*, vol. 17, pp. 647–657, 2006.

[23] D. Singh, S. Chaudhary, and C. Agarwal, "Corrosion characteristics of some aluminum alloys in nitric acid", *Journal of Electrochemical Science and Technology*, vol. 129, pp. 1869–1874, 1982.

[24] L. Zeng, D. T. Tran, C.-W. Tai, G. Svensson, and E. Olsson, "Atomic structure and oxygen deficiency of the ultrathin aluminium oxide barrier in Al/AlO_x/Al Josephson junctions", *Scientific Reports*, vol. 6, p. 29 679, 2016.

[25] *Aluminium etching*, `https://www.microchemicals.eu/technical_information/aluminium_etching.pdf`, Accessed: 2019-04-01, MicroChemicals.

[26] K. Williams and R. Muller, "Etch rates for micromachining processing", *Journal of Microelectromechanical Systems*, vol. 5, pp. 256–269, 1996.

[27] J. F. Cochran and D. E. Mapother, "Superconducting transition in aluminium", *Physical Review*, vol. 111, pp. 132–142, 1958.

[28] S. Probst, F. B. Song, P. A. Bushev, A. V. Ustinov, and M. Weides, "Efficient and robust analysis of complex scattering data under noise in microwave resonators", *Review of Scientific Instruments*, vol. 86, p. 024 706, 2015.

[29] I.-M. Svensson, "Tunable superconducting resonators", PhD thesis, Chalmers University of Technology, 2018.

[30] D. M. Pozar, *Microwave Engineering*, 4th ed. Wiley, 2012, ISBN: 978-0-470-63155-3.

[31] Y. Hou, R. Li, J. Liang, P. Su, and P. Ju, "Electropolishing of Al and Al alloys in $AlCl_3$/trimethylamine hydrochloride ionic liquid", *Surface & Coatings Technology*, vol. 335, pp. 72–79, 2018.